

# Structural relaxation in atomic clusters: Master equation dynamics

Mark A. Miller, Jonathan P. K. Doye and David J. Wales\*  
*University Chemical Laboratories, Lensfield Road, Cambridge CB2 1EW, UK*

The role of the potential energy landscape in determining the relaxation dynamics of model clusters is studied using a master equation. Two types of energy landscape are examined: a single funnel, as exemplified by 13-atom Morse clusters, and the double funnel landscape of the 38-atom Lennard-Jones cluster. Interwell rate constants are calculated using Rice–Ramsperger–Kassel–Marcus theory within the harmonic approximation, but anharmonic model partition functions are also considered. Decreasing the range of the potential in the Morse clusters is shown to hinder relaxation towards the global minimum, and this effect is related to the concomitant changes in the energy landscape. The relaxation modes that emerge from the master equation are interpreted and analysed to extract interfunnel rate constants for the Lennard-Jones cluster. Since this system is too large for a complete characterization of the energy landscape, the conditions under which the master equation can be applied to a limited database are explored. Connections are made to relaxation processes in proteins and structural glasses.

36.40.-c, 36.40.Ei, 61.46.+w

## I. INTRODUCTION

Some of the most interesting processes in chemical physics involve relaxation from a non-equilibrium state. Examples include the folding of a protein from a denatured conformation and the formation of a crystal or glass upon cooling a liquid. Given a method for calculating the rate constants for processes between mutually accessible states, the evolution of a non-equilibrium probability distribution can be described by a master equation [1].

A natural way to define a state in the master equation is provided by an “inherent structure” analysis of the potential energy surface (PES) [2]. Except at high temperatures, the configuration of an interacting system oscillates in the basin of attraction surrounding a local minimum on the PES, and sporadically undergoes transitions into neighbouring basins of attraction. A local minimum can therefore be regarded as a single state in the master equation, and transition states on the PES provide the means for dynamics to occur between the minima. We have recently obtained databases of minima and transition states for a variety of systems [3–6], providing the necessary ingredients for a master equation study. There are at least two advantages to modelling relaxation in this coarse-grained state-to-state way. Firstly, the master equation can usually be solved for much longer time scales than are accessible by direct simulations in which the equations of motion are integrated. Secondly, the master equation describes the relaxation of an ensemble without the need for explicit averaging over separate trajectories. In fact, the master equation can be used as a guide for simulations, for example to devise optimal annealing schedules [7].

In this contribution, the master equation is applied to structural databases that we have previously derived for some atomic clusters. Section II summarizes the master equation technique and methods for obtaining state-to-state rate constants in the microcanonical and canonical ensembles. Section III presents results for 13-atoms Morse clusters,  $M_{13}$ . The energy landscapes of these clusters each resemble a funnel, in which the minima are organized into pathways of decreasing energy that lead to the global minimum on the PES. The characteristics of the funnel change with the range of the potential, and have been studied in detail in previous work [4]. Section III also includes a discussion of harmonic and anharmonic partition function models for describing equilibrium properties of the clusters. In Sec. IV, dynamics on the paradigmatic double-funnel energy landscape of the 38-atom Lennard-Jones cluster,  $LJ_{38}$ , are studied. We have previously made a number of predictions concerning the dynamics of  $M_{13}$  [4] and  $LJ_{38}$  [5], which can now be examined. We will also present some new ways to interpret solutions of the master equation and extract information from them. The conditions under which the master equation treatment of interwell dynamics is valid will also be addressed, especially in the case of  $LJ_{38}$ , where the knowledge of the energy landscape is incomplete. Finally, Sec. V summarizes the main conclusions from this work.

## II. METHODS

---

\*Corresponding author

## A. The Master Equation

Let  $\mathbf{P}(t)$  be a vector whose components,  $P_i(t)$  ( $1 \leq i \leq n_{\min}$ ), are the probabilities of the cluster residing in a potential well of the geometrical isomer  $i$  at time  $t$ , the total number of such isomers being  $n_{\min}$ . The time evolution of these probabilities is governed by

$$\frac{dP_i(t)}{dt} = \sum_{j \neq i}^{n_{\min}} [k_{ij}P_j(t) - k_{ji}P_i(t)], \quad (1)$$

where  $k_{ij}$  is the first order rate constant for transitions from well  $j$  to well  $i$ . We can set up a transition matrix  $\mathbf{W}$ , with components

$$W_{ij} = k_{ij} - \delta_{ij} \sum_{m=1}^{n_{\min}} k_{mi}, \quad (2)$$

so that the diagonal components  $W_{ii}$  contain minus the total rate constant out of minimum  $i$ . This definition allows us to write the set of coupled linear differential equations (1)—the “master equation”—in matrix form:

$$\frac{d\mathbf{P}(t)}{dt} = \mathbf{W}\mathbf{P}(t). \quad (3)$$

If  $\mathbf{W}$  cannot be decomposed into block form then the system has a uniquely defined equilibrium state,  $\mathbf{P}^{\text{eq}}$ , for which  $(d\mathbf{P}/dt)|_{\mathbf{P}=\mathbf{P}^{\text{eq}}} = 0$ , i.e.,  $\mathbf{W}$  has a single zero eigenvalue whose eigenvector is the equilibrium probability distribution.  $\mathbf{W}$  is asymmetric, but can be symmetrized using the condition of detailed balance: at equilibrium,

$$W_{ij}P_j^{\text{eq}} = W_{ji}P_i^{\text{eq}}, \quad (4)$$

so that  $\tilde{W}_{ij} = (P_j^{\text{eq}}/P_i^{\text{eq}})^{1/2}W_{ij}$  is symmetric.  $\mathbf{W}$  and  $\tilde{\mathbf{W}}$  have the same eigenvalues,  $\lambda_i$ , and their respective normalized eigenvectors  $\mathbf{u}^{(i)}$  and  $\tilde{\mathbf{u}}^{(i)}$  are related by  $\mathbf{u}^{(i)} = \mathbf{S}\tilde{\mathbf{u}}^{(i)}$ , where  $\mathbf{S}$  is the diagonal matrix  $S_{ii} = \sqrt{P_i^{\text{eq}}}$ . Hence, individual components of the eigenvectors are related by  $u_j^{(i)} = \tilde{u}_j^{(i)}\sqrt{P_j^{\text{eq}}}$ . The solution of Eq. (3) is then [1,8]

$$P_i(t) = \sqrt{P_i^{\text{eq}}} \sum_{j=1}^{n_{\min}} \tilde{u}_i^{(j)} e^{\lambda_j t} \left[ \sum_{m=1}^{n_{\min}} \tilde{u}_m^{(j)} \frac{P_m(0)}{\sqrt{P_m^{\text{eq}}}} \right], \quad (5)$$

where  $\tilde{u}_m^{(j)}$  is component  $m$  of  $\tilde{\mathbf{u}}^{(j)}$ .

Apart from the zero eigenvalue, all the  $\lambda_j$  are negative [1]. We label eigenvalues and eigenvectors in order of decreasing algebraic value of the eigenvalue, so that  $\lambda_1 = 0$ , and  $\lambda_j < 0$  for  $2 \leq j \leq n_{\min}$ . As  $t \rightarrow \infty$ , only the  $j = 1$  term in Eq. (5) survives, and  $\mathbf{P}(t) \rightarrow \mathbf{P}^{\text{eq}}$ . This limit defines the baseline to which the remaining modes decay exponentially. The size of the contribution of mode  $j$  to the evolution of the probability of minimum  $i$  depends on component  $i$  of eigenvector  $j$ , and on a weighted overlap

between the initial probability vector and eigenvector  $j$ , i.e., the term in square brackets in Eq. (5). The sign of the product of these two quantities determines whether the mode makes an increasing or decreasing contribution with time. Combinations of modes with different signs give rise to the possibility of the accumulation and subsequent decay of transient populations as probability flows from the initial state to equilibrium via intermediates.

Eq. (5) requires the diagonalisation of the matrix  $\tilde{\mathbf{W}}$ , whose dimension is the number of minima in the database,  $n_{\min}$ . The time required to compute the eigenvectors scales as the cube of the dimension, and the storage requirements scale as its square. (Although  $\tilde{\mathbf{W}}$  may be sparse, its eigenvectors are not.) However, once diagonalisation has been achieved,  $P_i(t)$  can be calculated independently for any minimum  $i$  at any instant  $t$ . The only restriction on  $t$  comes from the accuracy to which the eigenvalues,  $\lambda_i$ , can be obtained; if the error is of the order  $\delta\lambda$ , Eq. (5) may diverge as  $t$  approaches  $1/\delta\lambda$ .

An alternative way of solving the master equation is to integrate Eq. (3) numerically. This approach has the advantage of not requiring diagonalisation of  $\tilde{\mathbf{W}}$ , and is therefore the only way to proceed for large databases. However, it has a number of disadvantages. Firstly, knowledge of the eigenvalues and eigenvectors of  $\tilde{\mathbf{W}}$  is useful in interpreting the time evolution of  $\mathbf{P}(t)$ . Secondly, accurate integration over long periods can be very slow, since the accumulation of numerical error can cause the sum of the probabilities to diverge rapidly. Thirdly, the full probability vector  $\mathbf{P}(t)$  (rather than selected components) must be propagated, and the integration must start from the time at which the initial probabilities are specified.

If the initial probability vector,  $\mathbf{P}(0)$ , is strongly non-equilibrium, many components of  $\mathbf{P}(t)$  change rapidly as soon as the integration starts, and then relax more slowly towards equilibrium. Therefore, when numerically integrating the master equation, the step size required for a given accuracy is usually smaller when  $t$  is closer to zero, and can be enlarged as  $t$  grows. To take advantage of this, the numerical integration in the present work was performed using a Bulirsch-Stoer algorithm with an adaptive step size [9]. Results from this method coincided precisely with those of the analytic solution, where the latter could be determined.

The linearity of the master equation rests on the assumption that the underlying dynamics are Markovian. The probability of the transition  $i \rightarrow j$  must not depend on the history of reaching minimum  $i$ , so that the elements of the transition matrix are indeed constants for a given temperature or total energy. For this restriction to apply, states within a potential well must equilibrate on a time scale faster than transitions to different minima, so that the transitions are truly stochastic. Previous results for other clusters [10,11] suggest that intrawell equilibration is quite rapid. The Markovian requirement will impose an upper limit to the temperatures at which the

master equation can be applied to transitions between minima, since at high temperatures the phase point does not reside in any one well long enough to establish equilibrium within it. Division of configuration space into the basins of attraction surrounding the minima is less useful in this dynamical regime.

### B. Rate Constants and Equilibrium Properties

To model the probability flow within a database of minima using the master equation requires knowledge of the rate constants,  $k_{ij}$ , for their interconversion. For the path from minimum  $j$  through a particular transition state, denoted  $\dagger$ , a general form for the rate constant is provided by RRKM theory [12]

$$k_j^\dagger(E) = \frac{W^\dagger(E)}{h\Omega_j(E)}. \quad (6)$$

Here,  $\Omega_j(E)$  is the density of states associated with minimum  $j$ , and

$$W^\dagger(E) = \int_{V^\dagger}^E \Omega^\dagger(E') dE' \quad (7)$$

is the sum of states at the transition state with the reactive mode removed;  $\Omega^\dagger(E)$  is the density of states at the transition state excluding this mode, and  $V^\dagger$  is the potential energy of the transition state. The total rate constant,  $k_{ij}$ , for the process  $j \rightarrow i$ , is then obtained by summing Eq. (6) over all transition states linking  $j$  and  $i$ .

Rates in the canonical ensemble, i.e., as a function of temperature rather than energy, can be obtained from Eq. (6) by Boltzmann weighting thus:

$$k_j^\dagger(T) = \frac{\int_{V^\dagger}^\infty k_j^\dagger(E) \Omega_j(E) e^{-E/k_B T} dE}{\int_{V_j}^\infty \Omega_j(E) e^{-E/k_B T} dE}, \quad (8)$$

where  $V_j$  is the potential energy of minimum  $j$ . Since the Laplace transforms

$$Z_j(T) = \int_{V_j}^\infty \Omega_j(E) e^{-E/k_B T} dE \quad (9)$$

and

$$Z^\dagger(T) = \int_{V^\dagger}^\infty \Omega^\dagger(E) e^{-E/k_B T} dE \quad (10)$$

are the vibrational partition functions of the minimum and transition state respectively, we obtain

$$k_j^\dagger(T) = \frac{k_B T}{h} \frac{Z^\dagger(T)}{Z_j(T)}. \quad (11)$$

Assigning a density of states or partition function to each minimum implies that the equilibrium properties of

the system are described by the superposition principle [13–15]. The total density of states and partition function are given by

$$\Omega(E) = \sum_{i=1}^{n_{\min}} \Omega_i(E) \quad \text{and} \quad Z(T) = \sum_{i=1}^{n_{\min}} Z_i(T). \quad (12)$$

Application of detailed balance to Eqs. (6) and (11) supplies the equilibrium occupation probabilities in the microcanonical and canonical ensembles:

$$P_i^{\text{eq}}(E) = \Omega_i(E)/\Omega(E), \quad P_i^{\text{eq}}(T) = Z_i(T)/Z(T). \quad (13)$$

These components emerge from the master equation as  $t \rightarrow \infty$ .

The use of  $\Omega_i(E)$  and  $Z_i(T)$  to calculate rates for the master equation when  $\mathbf{P} \neq \mathbf{P}^{\text{eq}}$  [i.e., when Eqs. (13) do not hold] still requires thermal equilibration of phase points *within* each potential well. This condition is fulfilled under the time scale separation of inter- and intrawell motion mentioned at the end of Sec. II A.

### III. MORSE CLUSTERS

In this section, we apply the master equation to databases derived for the 13-atom Morse cluster,  $M_{13}$ . The Morse potential [16] can be written as

$$V = \sum_{i < j} V_{ij}; \quad V_{ij} = e^{\rho(1-r_{ij}/r_e)} [e^{\rho(1-r_{ij}/r_e)} - 2]\epsilon, \quad (14)$$

where  $r_e$  and  $\epsilon$  are the dimer pair separation and well depth respectively.  $\rho$  is a dimensionless parameter which determines the range of the interparticle forces, with small  $\rho$  corresponding to long range. Physically meaningful values include  $\rho = 3.15$  and  $3.17$  for sodium and potassium [17] up to about  $14$  for  $C_{60}$  molecules [18,19]. When  $\rho = 6$ , the Morse potential has the same curvature as the Lennard-Jones potential at the minimum.  $\epsilon$ ,  $r_e$  and the atomic mass,  $m$ , define the system of reduced units for the Morse potential independently of  $\rho$ , giving  $(mr_e^2/\epsilon)^{1/2}$  as the reduced unit of time.

Details of databases obtained for four values of  $\rho$  have been given previously [4]. They demonstrate that the energy landscape of these clusters is a single funnel—a collection of kinetic pathways leading to a particular low-energy structure. However, the funnel has a steeper energetic gradient and lower downhill barriers when the range of the potential is long. The number of stationary points increases dramatically as the range is decreased, and the system must then overcome more barriers to reach the global minimum. These effects are expected to hinder relaxation towards the global minimum. In Sec. A, we examine the performance of some partition function models for the equilibrium properties of the clusters, before addressing the dynamics in Sec. B.

## A. Partition Function Models

The ingredients for the equations of Sec. II B are the densities of states for each minimum and transition state. If the harmonic approximation is applied to the vibrational density of states of a one-component  $N$ -atom cluster, the result is

$$\Omega_i^{\text{HO}}(E) = \frac{2N!}{h_i^{\text{PG}}} \frac{(E - V_i)^{\kappa-1}}{(\kappa-1)! (h\bar{\nu}_i)^{\kappa}}, \quad (15)$$

where  $\bar{\nu}$  is the geometric mean frequency,  $\kappa = 3N - 6$  is the number of vibrational degrees of freedom and  $h_i^{\text{PG}}$  is the order of the point group of the isomer. The corresponding partition function is

$$Z_i^{\text{HO}}(T) = \frac{2N!}{h_i^{\text{PG}}} \frac{(k_{\text{B}}T)^{\kappa}}{(h\bar{\nu}_i)^{\kappa}} e^{-V_i/k_{\text{B}}T}. \quad (16)$$

Eqs. (15) and (16) can be applied to transition states by excluding the reactive mode, in which case  $\kappa = 3N - 7$ .

The harmonic treatment is approximate in two ways. Firstly, the anharmonicity of the potential is ignored. Secondly, the density of states around each minimum is modelled as the surface area of a hyperellipsoid in phase space, and the overlap of the hyperellipsoids belonging to different minima is neglected. Both these effects become more pronounced as the total energy increases; highly anharmonic barrier regions are reached, and the phase space hyperellipsoids become larger.

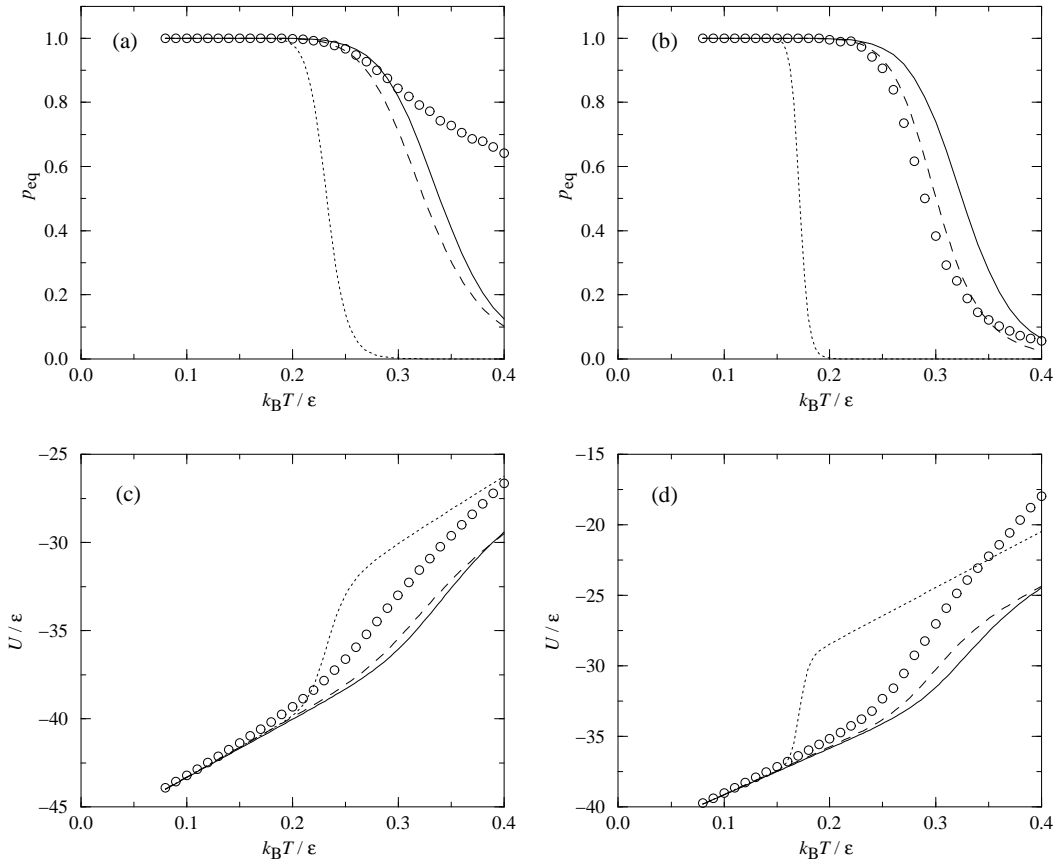


FIG. 1. Equilibrium occupation probability of the global minimum (top row) and canonical caloric curves (bottom row) for  $M_{13}$  with  $\rho = 4$  (left column) and  $\rho = 6$  (right column). Circles: canonical MC simulations, solid lines: harmonic approximation, dotted lines: MB method, dashed lines: MB( $\eta_{\text{P}} = 0.1$ ) method (see text).

A simple test of the partition function model is to compare the equilibrium probability of the global minimum predicted by Eqs. (13) with the fraction of quenches to this structure in the course of a simulation. We have observed elsewhere [11] that the harmonic approximation works quite well for the equilibrium probabilities of LJ<sub>7</sub> isomers in the microcanonical ensemble, even in the liquid-like regime. Figures 1a and 1b show how the har-

monic approximation performs for the global minimum of the  $M_{13}$  clusters with  $\rho = 4$  and 6 in the canonical ensemble, using the databases obtained previously [4]. The graphs also show the equilibrium probability of the global minimum obtained by quenching from canonical Monte Carlo (MC) simulations. In the simulations, a spherical container of radius  $3\sigma$  was imposed to prevent evaporation. At each temperature  $2 \times 10^6$  single-particle warm-up

steps were performed before collecting data over  $2 \times 10^8$  steps, quenching every  $10^4$  steps to find the local minimum in which the phase point resided. The harmonic curves depart from the MC results soon after the cluster begins to melt. For  $\rho = 6$  (Fig. 1b), the harmonic curve has the correct qualitative shape, but is shifted to higher temperature. For  $\rho = 4$  (Fig. 1a), however, the harmonic approximation underestimates the MC result increasingly badly above about  $k_B T = 0.3 \epsilon$ .

The modelling of partition functions of individual minima for use in the master equation has been the subject of an extensive study by Ball and Berry [20,21]. These authors considered a variety of analytic forms for  $Z_i(T)$  which attempt to improve on the shortcomings of the harmonic approximation. The greatest improvement was produced using an anharmonic model based on a first order expansion of the density of states for the Morse potential [22,23]. The anharmonic correction for each minimum was derived from the heights of the barriers connected to it. The resulting partition function for this ‘‘Morse barrier’’ (MB) method is

$$Z_i^{\text{MB}}(T) = Z_i^{\text{HO}} \prod_{j=1}^{n_i} \left(1 + a_j^{(i)} k_B T\right)^{\alpha_i}. \quad (17)$$

In this expression,  $n_i$  is the number of transition states connected to minimum  $i$ , and  $a_j^{(i)} = (2\Delta V_j^{(i)})^{-1}$  is the anharmonicity parameter derived from the barrier height,  $\Delta V_j^{(i)}$ , of the  $j$ th transition state connected to minimum  $i$ . The power  $\alpha_i = \min[1, \kappa/n_i]$  compensates for the possibility that there may be more than  $\kappa$  transition states connected to a given minimum, since the original model on which Eq. (17) is based associated one barrier with each normal mode. The MB model experiences problems when minima are connected by low barriers because the full series for the density of states of a Morse oscillator, from which the partition function is derived, diverges as  $k_B T$  approaches  $\Delta V_j^{(i)}$ . This behaviour correctly corresponds to dissociation of the Morse oscillator, but for a cluster isomerisation the density of states should remain finite above the barrier. Ball and Berry [20] suggested two ways to circumvent this difficulty. In the first approach, anharmonic corrections were applied only to low-energy minima, which tend not to have small barriers. This prescription is not entirely satisfactory because the low barriers of high-energy minima are a signature of the strong anharmonicity in these states, which is then ignored by this method. Furthermore, some criterion for selecting minima for anharmonic corrections is required. The second method, called MB( $\eta_P$ ), involved limiting the anharmonic correction  $a_j^{(i)} k_B T$  for each barrier to a plateau value,  $\eta_P$ , at temperatures where it would exceed this value, i.e.,

$$Z_i^{\text{MB}(\eta_P)}(T) = Z_i^{\text{HO}} \prod_{j=1}^{n_i} \left(1 + \min\left[\eta_P, a_j^{(i)} k_B T\right]\right)^{\alpha_i}. \quad (18)$$

Although a reasonable value of  $\eta_P$  might be expected to be around 0.5 (i.e., where  $k_B T = \Delta V_j^{(i)}$ ), the best agreement with quenching from constant temperature molecular dynamics (MD) simulations was achieved for  $\eta_P \approx 0.1$ .

The global minimum equilibrium probabilities of the  $M_{13}$  clusters with  $\rho = 4$  and 6 using the MB and MB( $\eta_P$ ) formulations are shown by the dotted and dashed lines in Figs. 1a and 1b. The inadequacy of the unconstrained MB model is obvious; the large anharmonic corrections of the high-energy minima cause these states to dominate as soon as they become energetically accessible, making the probability of the global minimum plummet at an artificially low temperature. For  $\rho = 4$ , the MB( $\eta_P$ ) model produces a marginally better match to the MC data at low temperature than the harmonic approximation, but then deviates more rapidly. For  $\rho = 6$ , quite a reasonable improvement is achieved. However, the position of the curve is continuously adjustable from the MB method (effectively  $\eta_P = \infty$ ) to the harmonic approximation ( $\eta_P = 0$ ), so it is difficult to argue that the improvement is based on physical insight.

The effect of the partition function model on the equilibrium probabilities of minima other than the global minimum is hard to gauge for a system where there are so many of them, since the quench statistics are poor. However, an impression of the overall description of the PES can be gained through thermodynamic properties derived from the superposition method. The internal energy can be obtained from the standard relation  $U = k_B T^2 (\partial \ln Z / \partial T)_{N,V}$ . The harmonic approximation yields the classical equipartition result

$$U^{\text{HO}} = \frac{1}{Z^{\text{HO}}} \sum_{i=1}^{n_{\text{min}}} Z_i^{\text{HO}} (V_i + \kappa k_B T), \quad (19)$$

and the MB( $\eta_P$ ) model [Eq. (18)] gives

$$U^{\text{MB}(\eta_P)} = \frac{1}{Z^{\text{MB}(\eta_P)}} \sum_{i=1}^{n_{\text{min}}} Z_i^{\text{MB}(\eta_P)} \left[ V_i + \kappa k_B T + \alpha_i (k_B T)^2 \sum_{j=1}^{n_i} \frac{a_j^{(i)} \Theta\left(\eta_P - a_j^{(i)} k_B T\right)}{1 + a_j^{(i)} k_B T} \right], \quad (20)$$

where the step function signifies that the derivative of the anharmonic correction from a given mode to the partition function is zero once the plateau has been reached. The derivative is also assumed to vanish at the point  $a_j^{(i)} k_B T = \eta_P$ , where the plateau starts, even though it is really discontinuous.

Figures 1c and 1d compare the canonical caloric curves of  $M_{13}$  with  $\rho = 4$  and 6 given by Eqs. (19) and (20). Also shown are the results from MC simulation, obtained by adding the kinetic contribution  $\kappa k_B T/2$  to the configurational part given by the simulations. For both clusters, the harmonic approximation underestimates the internal energy. The MB method incorrectly predicts a

sharp transition at the temperatures where the equilibrium probability shifts from the global minimum in Figs. 1a and 1b. The MB( $\eta_P = 0.1$ ) method, however, represents only a marginal improvement on the harmonic approximation. We have also found this to be the case for the LJ<sub>9</sub> cluster studied by Ball and Berry [20], using the model that gave the greatest improvement for the equilibrium probabilities of the various isomers. This result shows that optimizing the models for the probabilities does not necessarily produce the correct thermodynamic behaviour. Doye and Wales found that, whilst first order anharmonic corrections were enough to improve the thermodynamic description of LJ<sub>55</sub> in the superposition method, second order corrections were necessary for the smaller LJ<sub>13</sub> [23].

Attempts to model the density of states of individual minima using an analytic function of the energy implicitly assume that the “shape” of the basin of attraction is simple enough to be described adequately by such a form. In practice, basins of attraction are probably highly complex objects. For example, in previous work [4] we saw that increasing the range of the potential removes locally stable minima, but remnants of these features are likely to persist as shoulders or inflections on the PES, so that regions of configuration space that were associated with shallow minima for a shorter-ranged potential become formally associated with other minima when the range is increased. These features might explain why the model partition function results in Fig. 1 are worse for  $\rho = 4$  than for  $\rho = 6$ .

To illustrate this effect, we have performed microcanonical MD simulations of M<sub>13</sub> with  $\rho = 4$ , and LJ<sub>13</sub>, which closely resembles M<sub>13</sub> with  $\rho = 6$ . Periodic quenching was applied, and the Euclidean distance,  $D$ , was calculated between the configuration point taken at the start of the quench and the local minimum to which it converged. The distribution of  $D$  for the subset of quenches that led to the global minimum is plotted in Fig. 2 at two energies for each cluster. In each case, the lower energy has been chosen just above that at which the trajectory can escape from the global minimum, so that over 95% of quenches return to the global minimum, and the cluster is exploring a large proportion of the catchment basin of this structure. The higher energy was chosen such that about half the quenches return to the global minimum. The corresponding distributions are broader and peak at a higher value of  $D$ , as would be expected. The shaded region on each graph shows the distribution of  $D$  for the minima directly connected to the global minimum. Each of these minima is surrounded by its own basin of attraction, and a barrier must be surmounted before the configuration point enters the catchment basin of the global minimum. Even so, in Fig. 2b for LJ<sub>13</sub>, the tail of the high-energy quench distribution overlaps somewhat with the distribution of connected minima, indicating that some of the points in the basin of attraction of the global minimum are as far from it as the closest local minima. In Fig. 2a for M<sub>13</sub> with  $\rho = 4$ , however,

the high-energy quench distribution overlaps completely with the distribution of connected minima. The overlap means that many configurations which differ structurally from the global minimum as much as the connected local minima still quench to the global minimum. Such configurations may include structures which for a slightly shorter-ranged potential fall into the catchment basin of a different local minimum.

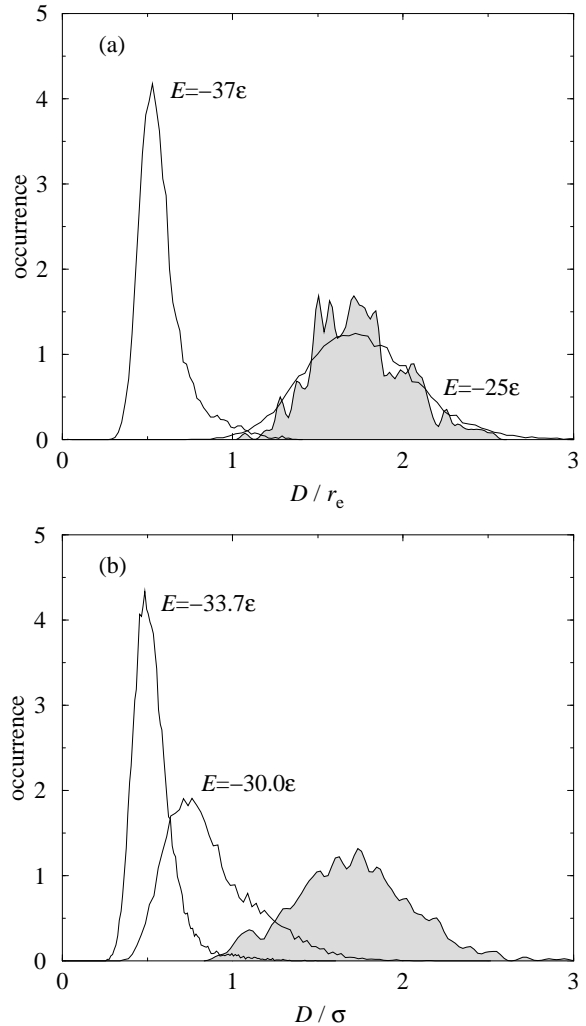


FIG. 2. Distribution of Euclidean distances to the global minimum from configuration points in its basin of attraction for (a) M<sub>13</sub>,  $\rho = 4$  and (b) LJ<sub>13</sub>. For each cluster, the distributions from microcanonical MD simulations at two energies are shown. At the lower energy, the majority of quenches lead to the global minimum, and at the higher energy, about half do so. The quench interval was 15 reduced time units. The duration of the high-energy simulations was  $6 \times 10^5$ , and that of the low-energy ones was  $3 \times 10^5$ . The shaded areas show the distance distribution of minima that are directly connected to the global minimum.

Further evidence to support this explanation comes from Fig. 1. The MC results for  $\rho = 6$  show that the increase in gradient of the caloric curve—indicative of the

system sampling a new region of configuration space—occurs at the temperature where the trajectory begins to escape from the global minimum, as shown by the decrease in  $P_{\text{gmin}}^{\text{eq}}$ . The transition is therefore out of the basin of attraction of the global minimum, effectively from solid-like to liquid-like states. The analogous results for  $\rho = 4$  show that the transition feature in the caloric curve starts before the probability of the global minimum drops significantly. This behaviour is suggestive of a weak transition from configurations close to the global minimum to higher-energy ones, all taking place within the basin of attraction of the global minimum itself.

The picture of the basin of attraction around the global minimum that emerges is therefore complex. It extends

far into configuration space from the icosahedron, and past the catchment basins of local minima in certain directions. The structural dissimilarity of some points which are formally associated with the global minimum suggests that quenching might not be the most meaningful way of dividing configuration space amongst the various minima. From this point of view, the underestimation of the global minimum probability in Fig. 1a by the harmonic superposition method is somewhat misleading, since it is not helpful to think of the distant configurations as belonging to the icosahedral well. The harmonic approximation may therefore give a more meaningful probability that the cluster has a structure resembling the global minimum than quenching.

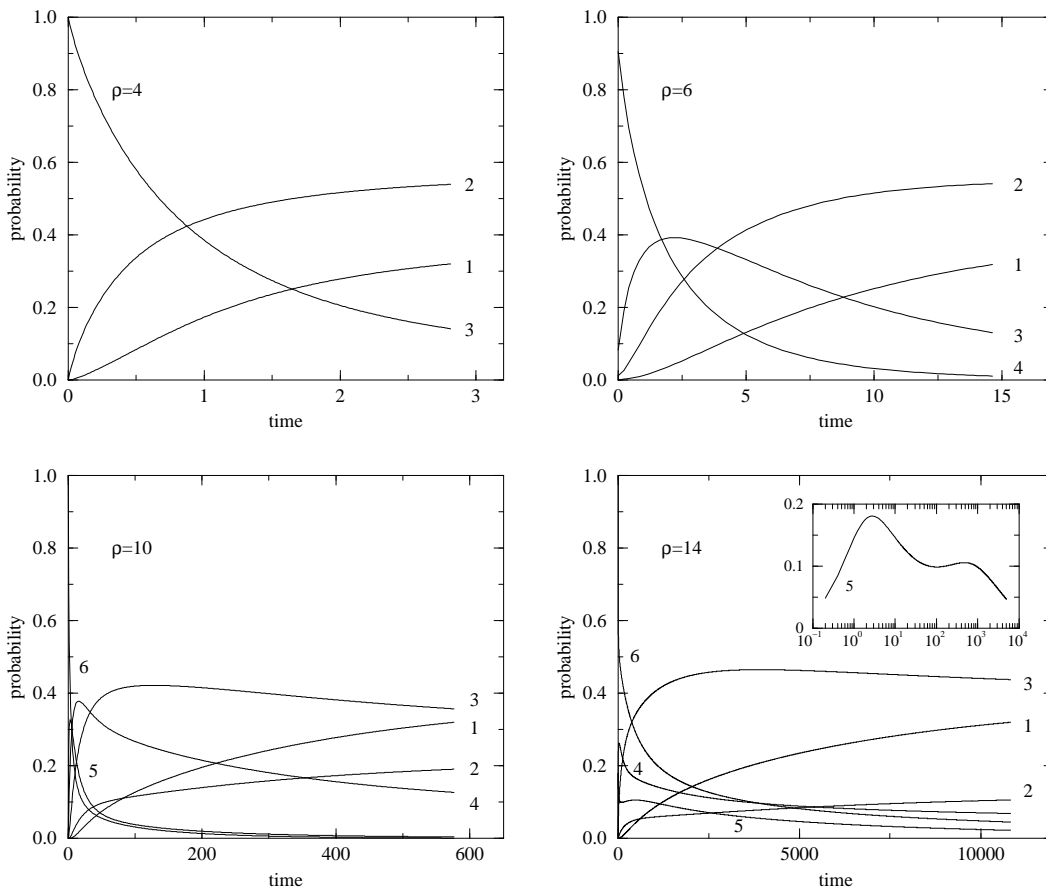


FIG. 3. Relaxation of minima, grouped in “layers” away from the global minimum, for  $M_{13}$  at four values of the range parameter,  $\rho$ . In each plot, layer 1 is the global minimum, layer 2 contains all minima directly connected to layer 1, etc. In each case, the microcanonical total energy is chosen such that the equilibrium probability of the global minimum is 0.4: for  $\rho = 4, 6, 10, 14$ ,  $E/\epsilon = -33.17, -29.42, -28.43, -29.78$ , respectively. The inset for  $\rho = 14$  shows the first half of the layer 5 curve with a logarithmic time axis. The time is in units of  $(mr_e^2/\epsilon)^{1/2}$ .

In summary, although the harmonic approximation has only partial success in describing the equilibrium properties of the clusters examined here, it is attractive in its simplicity, lack of empirical parameters, and clear physical basis. More complicated analytic models do not nec-

essarily provide greater insight, or even systematically improved results. We therefore adopt the harmonic approximation for the rate constant and equilibrium property expressions in Sec. II B, with the proviso that they will only be applied at low and moderate temperatures,

where the description should be adequate for our purposes. The resulting microcanonical rate constants, via Eq. (6), are given by

$$k_i^\dagger(E) = \frac{h_i^{\text{PG}}}{h^{\text{PG}\dagger}} \frac{\bar{\nu}_i^\kappa}{\bar{\nu}^\dagger(\kappa-1)} \left( \frac{E - V^\dagger}{E - V_i} \right)^{\kappa-1}, \quad (21)$$

and the canonical expression from Eq. (11) is

$$k_j^\dagger(T) = \frac{h_j^{\text{PG}}}{h^{\text{PG}\dagger}} \frac{\bar{\nu}_i^\kappa}{\bar{\nu}^\dagger(\kappa-1)} e^{-(V^\dagger - V_j)/k_B T}. \quad (22)$$

Finally, we note that the harmonic superposition method is likely to be more successful in the canonical ensemble than the microcanonical because at constant temperature the velocity distribution is independent of the configuration point. In contrast, at fixed total energy the kinetic energy is significantly further “above” the PES when the configuration point is near a deep potential well than when it is near higher-lying ones.

## B. Relaxation and the Range of the Potential

### 1. Relaxation to the Global Minimum

We now turn to the effect of the range of the potential on the dynamics of the  $M_{13}$  clusters in the light of our previous analysis of the energy landscapes [4]. The larger number of rearrangements and smaller energy gradient on paths to the global minimum, as well as the higher downhill barriers, are expected to impede relaxation to the global minimum as the range of the potential is decreased.

Figure 3 illustrates the range dependence of structural relaxation to the global minimum. The minima are grouped into “layers” according to the smallest number of rearrangements required to reach the global minimum. Layer 1 contains only the global minimum, and level  $i+1$  contains all minima directly connected to a minimum in level  $i$ , but not to any minimum in a layer lower than  $i$ . The initial probability vector at each value of  $\rho$  is a uniform distribution amongst the minima in the furthest layer from the global minimum. The energy has been chosen such that the equilibrium probability of the global minimum is 0.4, and the solution of the master equation is shown until the time at which 80% of this population (i.e., 0.32) has been achieved.

The most striking trend is the increasing time scale as the potential range decreases, as predicted by the landscape analysis [4]. The  $\rho = 14$  cluster takes over three orders of magnitude longer to reach 80% of equilibrium than the  $\rho = 4$  cluster. Note that for the latter system, the time scale plotted is only of the order of a few vibrational periods [4]. In the light of previous work [11] the application of the master equation to the  $\rho = 4$  cluster is therefore probably at the limit of validity, since the

assumption of stochastic transitions breaks down when the relaxation time approaches the vibrational period.

The relaxation is straightforward for  $\rho = 4$ ; the furthest layer decays whilst the populations of the global minimum and the intermediate layer grow monotonically. At  $\rho = 6$  we see the accumulation and decay of a transient population in layer 3 as the outward flow from these minima does not match the rapid initial input from the furthest layer. The layer 3 minima therefore constitute a kinetic bottleneck for relaxation down the funnel of the PES. More complex behaviour arises for  $\rho = 10$  and 14, where there are six layers of minima. The probabilities experience an initial jump as the system is released from its strongly non-equilibrium state, and then relax slowly to their final values. Layer 5 at  $\rho = 14$  (shown in the inset of Fig. 3) shows particularly complicated behaviour, rising suddenly at first, decaying slightly, and then rising again before relaxing monotonically. This oscillation occurs because layer 4 develops a transient population, blocking further downward output from layer 5 while layer 6 is still releasing probability into layer 5 from above.

### 2. Search Times

By analogy with the “folding time” in the protein folding literature, we can examine the ability of the cluster to find its global minimum by defining a “search time” as the time taken for the probability of the global minimum to reach a particular value after the system is released from a non-equilibrium state. Here we use a probability threshold of 0.4, but we will discuss the effects of changing this choice.

Fig. 4 shows the search time for  $M_{13}$  as a function of temperature using four values of  $\rho$ . The initial probability vector was a uniform distribution amongst the minima in the layer furthest from the global minimum. The qualitative shape of the curves is easily understood. As the temperature is increased from low values, the search time decreases because the thermal energy rises above the barriers between the minima. An optimal temperature,  $T_{\text{opt}}$ , is reached, where the search time is a minimum,  $\tau_{\text{opt}}$ , above which it rises because the thermodynamic driving force towards the global minimum is reduced at higher temperatures. Ultimately, the equilibrium probability of the global minimum falls below the threshold of 0.4, and the search time is no longer defined. Similar behaviour has been observed for the same reasons in direct simulations of KCl clusters [24] and lattice protein models [25], as well as a master equation study of idealized energy landscapes [26].



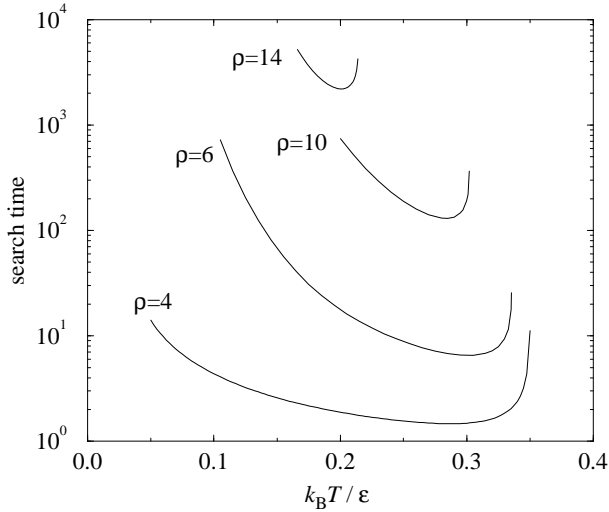


FIG. 4. Search time as a function of temperature for  $M_{13}$  at four values of the range parameter,  $\rho$ . The search time is defined as the time taken for the probability of the global minimum to reach 0.4, starting from an even probability distribution amongst the minima in the layer furthest from the global minimum. The time is in units of  $(mr_e^2/\epsilon)^{1/2}$ .

TABLE I. “Searching” characteristics of  $M_{13}$  at four values of the range parameter,  $\rho$ .  $T_{\text{opt}}$  is the optimal searching temperature, at which the search time is a minimum,  $\tau_{\text{opt}}$ .  $T_{\text{low}}$  and  $T_{\text{high}}$  ( $T_{\text{low}} < T_{\text{high}}$ ) are the two temperatures at which the search time equals  $2\tau_{\text{opt}}$ .

$\rho$	$k_B T_{\text{opt}}/\epsilon$	$\tau_{\text{opt}} / (mr_e^2/\epsilon)^{1/2}$	$k_B T_{\text{low}}/\epsilon$	$k_B T_{\text{high}}/\epsilon$	$\frac{T_{\text{opt}} - T_{\text{low}}}{T_{\text{high}} - T_{\text{low}}}$
4	0.293	1.47	0.135	0.344	0.76
6	0.305	6.54	0.218	0.333	0.76
10	0.285	130	0.235	0.301	0.76
14	0.200	2200	0.170	0.214	0.68

An analogy can be drawn here with the ease of folding in proteins. The ratio,  $T_f/T_g$ , of the “folding temperature” (where the native state becomes thermodynamically most stable) to the “glass transition temperature” (where the kinetics slow down dramatically) has been used as a measure of the ability of a protein to fold correctly [25,27].  $T_f$  is roughly related to  $T_{\text{high}}$ , which decreases with increasing  $\rho$ , whilst  $T_g$  increases because of the higher barriers for short-ranged potentials. Hence  $T_f/T_g$  falls, in accordance with the observation that searching for the global minimum is harder when  $\rho$  is high.

Interestingly, the curves in Fig. 4 for  $\rho = 4, 6$  and 10 have similar shapes. For example, the values of  $T_{\text{opt}}$  differ by only 7%. Furthermore,  $T_{\text{opt}}$  lies about three quarters of the way from  $T_{\text{low}}$  to  $T_{\text{high}}$  in all three cases, as shown by the last column of Table I.  $\rho = 14$  represents an extreme case in which relaxation to the global minimum becomes very slow for values outside a small range near  $T_{\text{opt}}$ . This optimum temperature is a com-

promise between the slow dynamics at even moderately low temperatures, and the rapidly decreasing thermodynamic weight of the global minimum at moderately high temperatures.

Table I lists the temperature and  $\tau_{\text{opt}}$ , as well as the two temperatures,  $T_{\text{low}}$  and  $T_{\text{high}}$ , at which the search time equals  $2\tau_{\text{opt}}$ . The difference  $T_{\text{high}} - T_{\text{low}}$  provides a measure of the width of the temperature window for which searching is reasonably fast. The value of  $\tau_{\text{opt}}$  increases with  $\rho$ , as expected from the relaxation profiles of the previous section, and this slowing down is accompanied by a decrease in the temperature width  $T_{\text{high}} - T_{\text{low}}$ . As the range of the potential is decreased, the energy gap between the global minimum and the other minima becomes smaller, and the energy range spanned by the minima narrows. Hence, other minima come into play at lower temperature, and the temperature at which the global minimum ceases to dominate the equilibrium populations is lower when the potential is short-ranged. This observation explains why  $T_{\text{high}}$  falls as  $\rho$  increases. For high  $\rho$ , the downhill barriers between minima are on average larger, so that as the temperature is decreased, isomerisation processes slow down more dramatically than for small  $\rho$ . Hence, the search time increases more rapidly as the temperature is lowered beyond  $T_{\text{opt}}$  when the potential is short-ranged, resulting in the narrower ranges of  $T_{\text{high}} - T_{\text{low}}$ .

Choosing a different occupation probability of the global minimum as the criterion for the search time has predictable effects. If a higher threshold is used, the search time increases at any given temperature. The equilibrium probability of the global minimum drops below the threshold at a lower temperature, so the upper limit for which the search time is defined decreases. The search time rises more steeply below  $T_{\text{opt}}$  because the probabilities must come closer to their equilibrium values, and this approach is asymptotic. The combined effect is that the search time curves all become narrower. However, for the cases tested ( $\rho = 4$  and 6),  $T_{\text{opt}}$  changed by only 10% as the threshold was varied from 0.2 to 0.5.

### 3. Relaxation of the Total Energy

The evolution of the probability vector towards  $\mathbf{P}^{\text{eq}}$  is expressed macroscopically by the relaxation of some overall property,  $A$ , to its equilibrium value,  $A^{\text{eq}}$ . If this property has a well defined value,  $A_i$ , for each state  $i$  in the master equation, the expectation value is a weighted average which can be expressed as a function of time using Eq. (5):

$$\langle A(t) \rangle = \sum_{i=1}^{n_{\min}} A_i P_i(t) = \sum_{j=1}^{n_{\min}} c_j e^{\lambda_j t} = A^{\text{eq}} + \sum_{j=2}^{n_{\min}} c_j e^{\lambda_j t}, \quad (23)$$

where

$$c_j = \left[ \sum_{i=1}^{n_{\min}} A_i \sqrt{P_i^{\text{eq}}} \tilde{u}_i^{(j)} \right] \left[ \sum_{m=1}^{n_{\min}} \tilde{u}_m^{(j)} \frac{P_m(0)}{\sqrt{P_m^{\text{eq}}}} \right], \quad (24)$$

and the last expression in Eq. (23) uses the fact that the  $j = 1$  term defines the baseline for relaxation, since  $\lambda_1 = 0$ . A mean relaxation time,  $\tau_r$ , can be defined by normalizing the profile of  $\langle A \rangle$  against  $t$  (such that it decays from 1 to 0), and evaluating the area under the resulting curve [28]. For pure Debye (single exponential) relaxation, i.e.,  $\exp(-\lambda t)$ , one simply obtains  $\tau_r = \lambda^{-1}$ . Subtracting the equilibrium value from the right-hand side of Eq. (23), integrating from  $t = 0$  to  $\infty$ , and normalizing using the value at  $t = 0$  yields

$$\tau_r = - \sum_{j=2}^{n_{\min}} c_j \lambda_j^{-1} / \sum_{j=2}^{n_{\min}} c_j. \quad (25)$$

If the eigenvectors and eigenvalues of the transition matrix are not available,  $\tau_r$  can be obtained by propagating the master equation numerically until  $\langle A \rangle$  has effectively equilibrated, and then numerically integrating the normalized relaxation profile. Here we will examine the relaxation of the total energy of  $M_{13}$  as the populations of the minima equilibrate at constant temperature. Within the harmonic approximation, therefore, we need  $A_i = V_i + \kappa k_B T$  in Eqs. (23) and (24).

Theoretical treatments have shown that under particular circumstances, the multi-exponential decay that arises from the master equation can lead to a variety of asymptotic behaviours. For example, the random energy model, where the states have a Gaussian distribution of energies, can lead either to stretched exponential ( $\propto \exp[-(t/\tau)^\theta]$ ) or to power law ( $\propto [\tau/t]^p$ ) relaxation of autocorrelation functions, depending on the form chosen for the transition rates [29]. Palmer et al. also derived stretched exponential behaviour for a hierarchically constrained model [30]. In contrast Skorobogatiy et al. found power law and logarithmic ( $\propto -\ln t$ ) decay, but not stretched exponential decay, of the total energy in a protein model [31], depending on the temperature.

Starting from a uniform distribution amongst the minima in the layer furthest from the global minimum, we found that none of the above forms (pure or stretched exponential, power law, or logarithmic) gave a robust fit to the decay of the total energy from the master equation. At sufficiently long times, Eq. (23) approaches pure exponential behaviour, since all contributions except that of the slowest mode have decayed. At intermediate times, the parameters (particularly the stretching exponent,  $\theta$ ) that produced the best fit for the stretched exponential form were highly sensitive to the time interval over which data were supplied, and the resulting curves often deviated significantly from the master equation solution. The difficulty of obtaining an acceptable fit increased with decreasing temperature, where the spread of the exponents  $\lambda_j$  is wider. Of course, there is no reason why a general multi-exponential form like Eq. (23) should conform to any simplified model.

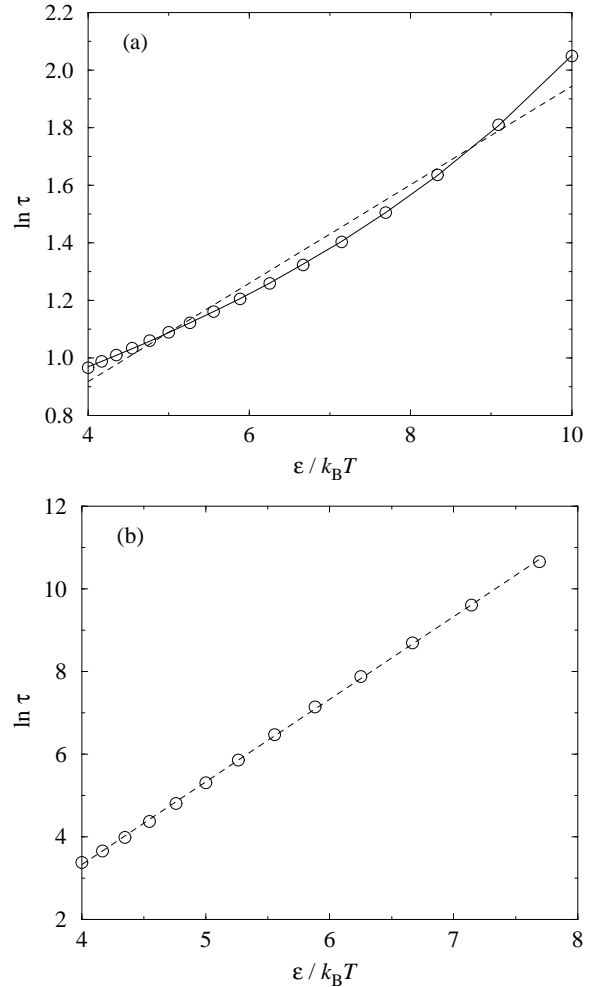


FIG. 5. Canonical ensemble Arrhenius plots for the relaxation time of the total energy of  $M_{13}$  at (a)  $\rho = 4$  and (b)  $\rho = 14$ . Circles are mean relaxation times from the master equation, dashed lines are fits to the Arrhenius form, and the solid line in (a) is a fit to the Vogel-Tammann-Fulcher (VTF) form. The relaxation time is in units of  $(mr_e^2/\epsilon)^{1/2}$ .

Although the relaxation profiles are complicated, the mean relaxation times (integrated profiles) were found to follow simple empirical expressions. Fig. III B 3 shows the logarithm of the relaxation time as a function of inverse temperature for  $M_{13}$  with  $\rho = 4$  and 14. The  $\rho = 14$  plot in Fig. III B 3b is well fitted by the Arrhenius form  $\tau_r = \tau_0 \exp(A/k_B T)$  with  $\tau_0 = 9.34 \times 10^{-3} (mr_e^2/\epsilon)^{1/2}$  and  $A = 2.00 \epsilon$ . The  $\rho = 4$  plot in Fig. III B 3a, however, shows significant deviation from the linearized Arrhenius expression. It is better fitted by the ubiquitous Vogel–Tammann–Fulcher (VTF) form [32]

$$\tau_r = \tau_0 \exp \left[ \frac{A}{k_B(T - T_0)} \right], \quad (26)$$

as shown by the solid line, for which the parameters are  $\tau_0 = 1.86 (mr_e^2/\epsilon)^{1/2}$ ,  $A = 0.0699 \epsilon$ ,  $k_B T_0 = 0.051 \epsilon$ . These values were found by least squares fitting of the logarithm of Eq. (26) with equally weighted points.

The slower relaxation and larger database for the  $\rho = 14$  cluster meant that it was not computationally feasible to extend Fig. III B 3b to lower temperature—the lowest point shown is at  $k_B T = 0.13 \epsilon$ —and it is possible that deviation from the Arrhenius behaviour would occur below this value. However, the curvature of the  $\rho = 4$  plot is clear over the same range, indicating that the relaxation dynamics of the two clusters respond differently to temperature changes. The origins of the difference probably stem from the decreasing slope of the energy landscape as the range of the potential is shortened. The energy intervals spanned by the minimum and transition state samples at higher  $\rho$  are narrower, making the landscape more uniform. This uniformity means that a change in the temperature has a similar effect on most of the individual interwell processes, each of which separately has an Arrhenius temperature dependence in the model we have used [Eq. (22)]. On the steeper landscape of the  $\rho = 4$  cluster, however, there is a greater spread of local minimum energies and barrier heights, so that as the temperature is lowered, some processes become “frozen out” before others, resulting in longer relaxation times than expected by extrapolation of the high-temperature behaviour.

In structural glasses, Arrhenius temperature dependence of relaxation times is associated with strong liquids, whereas VTF behaviour is indicative of fragility [33]. If this classification can be applied to clusters, the results of this section suggest that increasing the range of the potential introduces a degree of fragility. Stillinger’s picture of strong liquids having a “uniformly rough” energy landscape [28] is in line with our previous analysis [4], which showed that decreasing the range of the potential lowers the overall slope of the PES, leaving a flat but rough landscape.

#### 4. Relaxation Modes

Is the time scale of relaxation mostly determined by the slowest relaxation mode of the master equation, i.e., the least negative non-zero eigenvalue of the transition matrix, or is the process it describes relatively unimportant? Eqs. (23) and (24) show that the contribution of a given mode to the relaxation of a global property depends both on the property and on the initial probability distribution. However, we can still probe the nature of the probability flow described by a particular relaxation mode by comparing the size and sign of the components in the corresponding transition matrix eigenvector. Consider Eq. (5) for a particular value of  $j$ ; mode  $j$  makes an important contribution to the probability evolution of minimum  $i$  if  $u_i^{(j)}$ —or equivalently  $\sqrt{P_i^{\text{eq}}} \tilde{u}_i^{(j)}$ —is large in magnitude. The mode represents an overall flow *between* minima  $i$  and  $k$  if  $u_i^{(j)}$  and  $u_k^{(j)}$  have opposite signs.

The extreme eigenvalues and eigenvectors of the transition matrix can be obtained efficiently for large matrices using Lanczos iteration [34]. Inspection of the components of the eigenvectors for  $M_{13}$  at different values of  $\rho$  and different temperatures reveals some general trends. The extreme modes (i.e., the slowest and fastest) describe probability flow between a small number of minima, typically fewer than five. The fastest modes tend to be between minima that are directly connected by transition states. In contrast, the slowest modes are between unconnected minima, and probability flow involves intermediate minima. The slow modes tend to involve one highly populated minimum. Hence, if the initial probabilities of the other minima that feature in these relaxation modes (with eigenvector components of opposite sign) are far from their equilibrium values, the slow modes may limit the overall relaxation.

The number of minima participating in relaxation mode  $j$  can be measured using the index

$$\tilde{n}_j = \frac{\left( \sum_{i=1}^{n_{\min}} \left[ \tilde{u}_i^{(j)} \sqrt{P_i^{\text{eq}}} \right]^2 \right)^2}{\sum_{i=1}^{n_{\min}} \left[ \tilde{u}_i^{(j)} \sqrt{P_i^{\text{eq}}} \right]^4}, \quad (27)$$

which varies from 1 to  $n_{\min}$ . Figure 6 shows  $\tilde{n}_j$  as a function of the eigenvalue,  $\lambda_j$ , for all the relaxation modes of  $M_{13}$  with  $\rho = 6$  at two temperatures. As observed above, the number of minima involved in the fastest and slowest modes is small. Many intermediate modes only involve a small number of minima too, but the modes that describe more global flow are all clustered in the centre of the (logarithmic) scale. This pattern is more pronounced at the higher temperature.

In a typical application of the master equation, therefore, the initial processes involve rapid equilibration between small groups of minima that are adjacent in configuration space. This is followed by wider probability flow between larger groups of minima, and finally slow ad-

justment of the population of a few minima via processes involving multiple rearrangements.

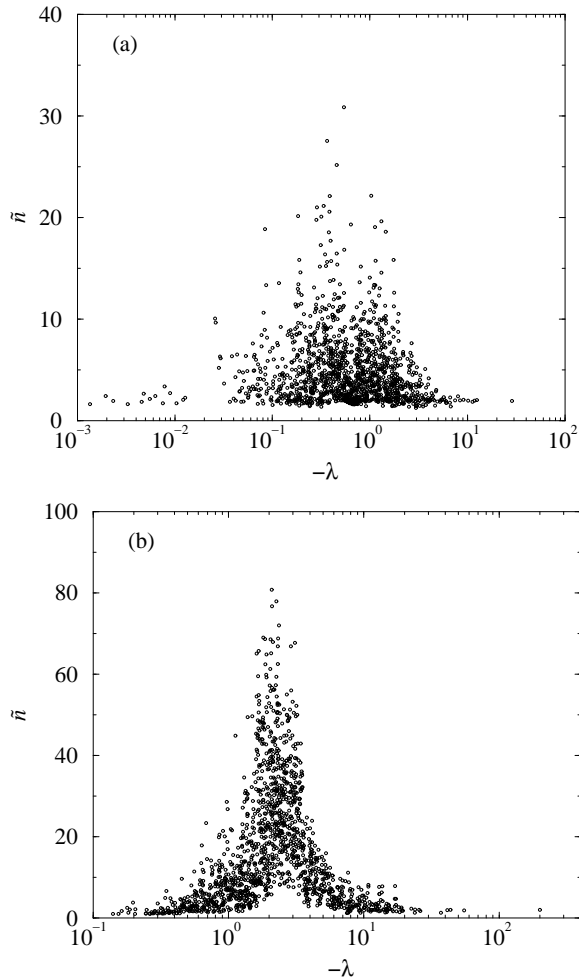


FIG. 6. Number of minima participating in a relaxation mode of the master equation as a function of the eigenvalue of the mode for  $M_{13}$ ,  $\rho = 6$ , at (a)  $k_B T = 0.15 \epsilon$  and (b)  $k_B T = 0.40 \epsilon$ . The mode with zero eigenvalue has been excluded.  $\lambda$  is in units of  $(\epsilon/mr_e^2)^{1/2}$ .

#### IV. INTERFUNNEL DYNAMICS IN $LJ_{38}$

We now turn to the double-funnel energy landscape of the 38-atom Lennard-Jones cluster,  $LJ_{38}$ . The potential energy is given by [35]

$$V = \sum_{i < j} V_{ij}; \quad V_{ij} = 4\epsilon \left[ \left( \frac{\sigma}{r_{ij}} \right)^{12} - \left( \frac{\sigma}{r_{ij}} \right)^6 \right], \quad (28)$$

where  $\sigma$  is the pair separation at which  $V_{ij} = 0$ , and  $\epsilon$  is the pair well depth. We will use  $\sigma$  and  $\epsilon$  as the units of the quantities they measure, setting both equal to unity; the topology of the PES is not affected by the values of these parameters.

The  $LJ_{38}$  cluster is too large for a complete catalogue of minima and transition states to be obtained. However, we have previously performed a thorough characterization of the low-energy regions of the PES using a database of 6000 minima and 8633 transition states [5,36]. The resulting disconnectivity graph [5,36] clearly showed two separated regions of configuration space, each having the character of a funnel. The global minimum lies at the bottom of a small funnel associated with 28 minima that are characterized by face-centred cubic packing. The larger funnel of 446 minima leads to the lowest-energy icosahedrally packed minimum. Since this secondary funnel accounts for a large volume of configuration space, and because the liquid-like minima are structurally more similar to the icosahedral minima than the fcc ones, the icosahedral funnel is expected to act as a kinetic trap for relaxation from high-energy states to the global minimum.

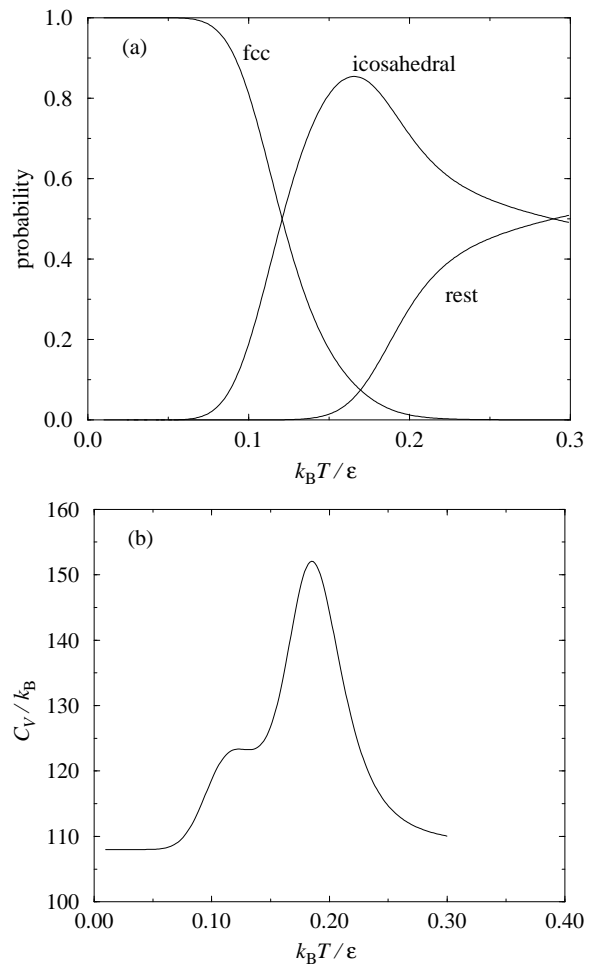


FIG. 7. Low-temperature properties of  $LJ_{38}$  calculated using the harmonic superposition approximation. (a) Equilibrium occupation probability of the fcc and icosahedral funnels and the rest of configuration space, and (b) the heat capacity.

By grouping together the minima in each of the two funnels, we can study not only equilibration within the funnels as for  $M_{13}$ , but also the dynamics between the funnels. Hence, we define the probabilities

$$P_{\text{fcc}}(t) = \sum_{i \in \text{fcc}} P_i(t) \quad \text{and} \quad P_{\text{icos}}(t) = \sum_{i \in \text{icos}} P_i(t). \quad (29)$$

The database obtained in previous work [5,36] is a good representation of the low-lying regions of the PES, but does not extend far into the liquid-like regime, and so we are restricted to studying the dynamics at low temperatures, where the role of the liquid is less important. This is not a serious restriction, since the time scale separation of inter- and intrafunnel processes should be greatest at low temperature.

To obtain an impression of the temperature range over which valid conclusions can be drawn, Fig. 7 presents some properties calculated using the harmonic superposition approximation and the full low-energy database of 6000 minima and 8633 transition states. Fig. 7a shows  $P_{\text{fcc}}^{\text{eq}}$  and  $P_{\text{icos}}^{\text{eq}}$  as a function of temperature. The global minimum only dominates at very low temperatures, since the larger number of minima and lower vibrational frequencies in the icosahedral funnel cause the phase volume of the latter to rise rapidly. At sufficiently high temperature the cluster should melt, and the occupation probabilities of the two funnels, which contain predominantly solid-like structures, should approach zero. However, the steady rise of the curve marked “rest” (i.e.,  $1 - P_{\text{fcc}} - P_{\text{icos}}$ ) is interrupted at  $k_B T \approx 0.2 \epsilon$ , reflecting the fact that the sample of minima does not represent the relevant regions of the PES very well above this temperature. Figure 7b shows the heat capacity, derived from  $C_V = (\partial U / \partial T)_V$  and Eq. (19). The small peak at  $k_B T \approx 0.12 \epsilon$  results from the transition from the fcc to icosahedral regions of configuration space, and the main peak at  $k_B T \approx 0.18 \epsilon$  signifies the melting transition. These features are largely in agreement with a more sophisticated anharmonic superposition method, which was designed to model the thermodynamics from a representative sample of minima [23,37]. The harmonic results presented here predict a lower peak for the melting transition, and beyond the melting temperature the heat capacity returns to its solid-like value. This result again reveals the deficiencies of the sample of minima in the liquid-like regime. We conclude, however, that as far as thermodynamic properties are concerned, the present sample should be adequate for  $k_B T < 0.2 \epsilon$ . The corresponding limit in the microcanonical ensemble is  $E < -150 \epsilon$ , and the fcc and icosahedral funnels have equal probability at  $E = -160.5 \epsilon$ . We note that conventional simulations would not be able to measure the quantities in Fig. 7 reliably at such temperatures because the interfunnel dynamics are too slow. One of the aims of this section is to quantify the rate of passage between the funnels.

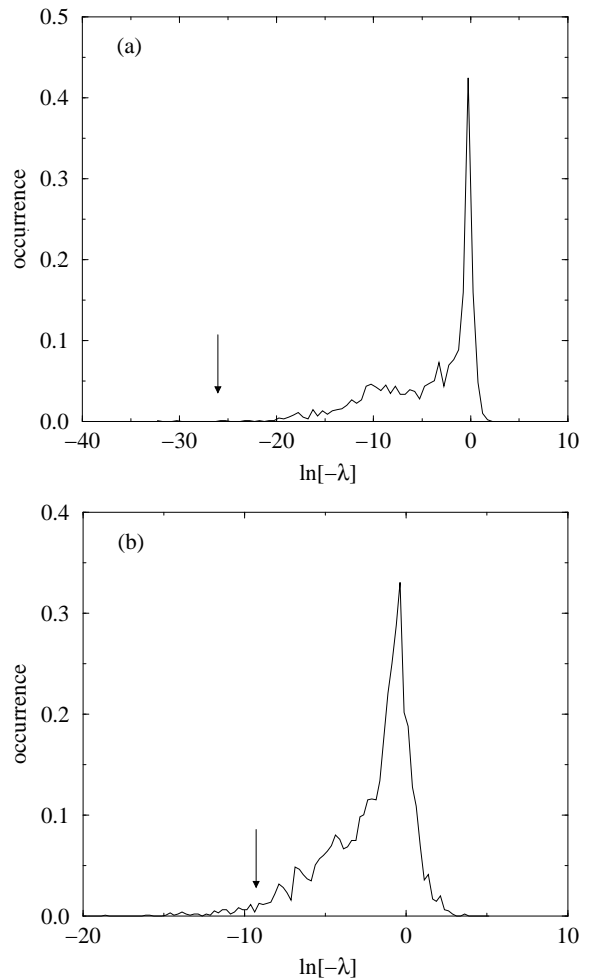


FIG. 8. Spectra of transition matrix eigenvalues for LJ<sub>38</sub> in the microcanonical ensemble at (a)  $E = -160 \epsilon$  and (b)  $E = -150 \epsilon$ . In each case, the eigenvalue of the most prominent interfunnel mode is marked by an arrow, showing the greater separation of its time scale from the other relaxation modes at low energy.  $\lambda$  is in units of  $(\epsilon/m\sigma^2)^{1/2}$ .

### A. Pruning the Database

Because the time scale of interfunnel processes is so long at low temperatures, numerical integration of the master equation is not feasible, so we must diagonalize the rate matrix and use Eq. (5). However, diagonalisation routines are likely to run into numerical problems when the matrix elements span many orders of magnitude. Fig. 8 shows that lowering the temperature widens the spread of eigenvalues. At sufficiently low temperature, a number of eigenvalues begin to appear to be slightly positive, or the diagonalisation routines may fail altogether. Czerminski and Elber reported similar problems [8], and therefore restricted their studies to sufficiently high temperatures. In Sec. III B we saw that the eigenvalues at the extremes of the spectrum tend to be associated with probability flow between a small number

of minima. If these minima are kinetically isolated, they cause the transition matrix to become nearly decomposable, giving rise to the numerical difficulties. Since they do not participate in probability flow we should seek to exclude them. If they are not kinetically isolated, they will also appear in other, faster, relaxation modes.

From a practical point of view, even if the transition matrix can be diagonalized without numerical difficulty, it is worth considering whether all the minima play a significant role. If some can be discarded without affecting the relaxation, the size of the matrix can be reduced, saving computational effort. Because of the astronomical number of minima on the PES, a large proportion of the minima found in a partial search are only linked to one other minimum in the database. Within the restricted sample, these minima constitute “dead ends” for probability flow. They can act as buffers, absorbing and releasing probability as it flows towards equilibrium through the connected minimum, but they cannot act as pathways for flow *between* minima or larger regions of the PES. The dead-end minima in our sample tend to be high in energy since the search algorithm only explores connections from low-energy minima thoroughly. When a high-energy minimum is found, the upward move is rejected and the search continues from the original minimum, never returning to the high ones. When modelling the probability flow from the bottom of one funnel into the other, high-energy dead-end minima are unlikely to play an important role because their equilibrium probability is low and they do not mediate interfunnel flow.

These considerations suggest ways of pruning the database. First, dead-end minima were identified, and were found to constitute about 70% of the sample of 6000 minima. To eliminate the kinetically isolated minima at a given energy, the total outward rate constant was calculated for each dead-end minimum, and the minimum was discarded if the rate fell below a certain threshold. For example, at a total energy of  $E = -160\epsilon$ , the rate constants for individual processes span the range  $10^{-41}$  to  $10^0 (\epsilon/m\sigma^2)^{1/2}$ . Choosing a threshold of  $10^{-12}$ , which corresponds to a time scale of seconds for argon parameters, reduces the sample of minima to 5944. A threshold of  $10^{-10}$  reduces it to 5861. While this may be sufficient to remove numerical difficulties in the diagonalisation procedure, the matrices are still rather large.

Trimming the sample on the basis of equilibrium probabilities reduced the number of minima more dramatically. At  $E = -160\epsilon$ , discarding dead-end minima whose equilibrium probability was less than  $10^{-10}$  left just 1825 minima, and a threshold of  $10^{-8}$  left 1782. Clearly, the number of minima removed by such a method decreases with increasing energy, since higher-energy states then become more populated. We will gauge the effect of pruning the database by examining the sensitivity of the results to the choice of the threshold.

## B. Interfunnel Rate Constants

What is the rate of crossing between the fcc and icosahedral funnels? We have previously shown that interconversion of the fcc and icosahedral minima is a multiple-step process [5]—the lowest-energy path in our sample involves 13 successive rearrangements—but let us consider the overall scheme



with “forward” and “reverse” rate constants  $k_+$  and  $k_-$ . The rate of change of the occupation probability of the fcc funnel is accordingly

$$\frac{dP_{\text{fcc}}(t)}{dt} = -k_+ P_{\text{fcc}}(t) + k_- P_{\text{icos}}(t). \quad (31)$$

From Fig. 7, we see that at sufficiently low temperature only the two funnels are significantly occupied at equilibrium, as opposed to minima associated with the liquid-like state. Assuming that this is also the case away from equilibrium, provided that the initial probability is itself confined to the funnels, we can write

$$P_{\text{fcc}}(t) + P_{\text{icos}}(t) = 1. \quad (32)$$

Using Eq. (32) and the equilibrium relationship

$$k_+ P_{\text{fcc}}^{\text{eq}} = k_- P_{\text{icos}}^{\text{eq}}, \quad (33)$$

integration of Eq. (31) gives the basic result of first order kinetics for a two-state model:

$$\ln \left[ \frac{P_{\text{fcc}}(t) - P_{\text{fcc}}^{\text{eq}}}{P_{\text{fcc}}(0) - P_{\text{fcc}}^{\text{eq}}} \right] = -(k_+ + k_-)t. \quad (34)$$

Figure 9a shows plots of Eq. (34) and the analogous expression for  $P_{\text{icos}}(t)$  in the microcanonical ensemble at  $E = -160\epsilon$ , starting from the global minimum. The plots were obtained from the analytic solution of the master equation after removing all dead-end minima with an equilibrium probability of less than  $10^{-8}$ , as described in Sec. IV A. The two lines are straight and coincide, and the slope yields  $k_+ + k_- = 4.99 \times 10^{-12} (\epsilon/m\sigma^2)^{1/2}$ . This value closely matches one of the eigenvalues of the transition matrix,  $|\lambda_4| = 4.98 \times 10^{-12} (\epsilon/m\sigma^2)^{1/2}$ , suggesting that the corresponding eigenvector describes flow between the two funnels. The “net flow index” into or out of a funnel F produced by relaxation mode  $i$  of the master equation can be obtained by summing the components of eigenvector  $i$  that correspond to the minima belonging to F [38]:

$$f_i^{\text{F}} = \sum_{j \in \text{F}} \tilde{u}_j^{(i)} \sqrt{P_j^{\text{eq}}}. \quad (35)$$

If mode  $i$  represents probability flow between the funnels, then  $f_i^{\text{fcc}}$  and  $f_i^{\text{icos}}$  will be larger in magnitude than for other eigenvectors, and will have opposite signs, so that an increasing contribution is made to one funnel and a

decreasing contribution to the other, depending on the initial probability vector [see Eq. (5)]. At  $E = -160 \epsilon$ , for the mode whose eigenvalue matches  $-(k_+ + k_-)$ , we find  $f_4^{\text{fcc}} = 0.495$  and  $f_4^{\text{icos}} = -0.495$ . The next largest net flow index for the fcc funnel was  $f_{93}^{\text{fcc}} = 3.97 \times 10^{-4}$  (with a corresponding index for the icosahedral funnel of  $f_{93}^{\text{icos}} = 9.94 \times 10^{-7}$ ) and that for the icosahedral funnel was  $f_9^{\text{icos}} = -0.143$  (with a corresponding index for the fcc funnel of  $f_9^{\text{fcc}} = 4.38 \times 10^{-5}$ ). This result unambiguously identifies the fourth mode with interfunnel relaxation at this energy.

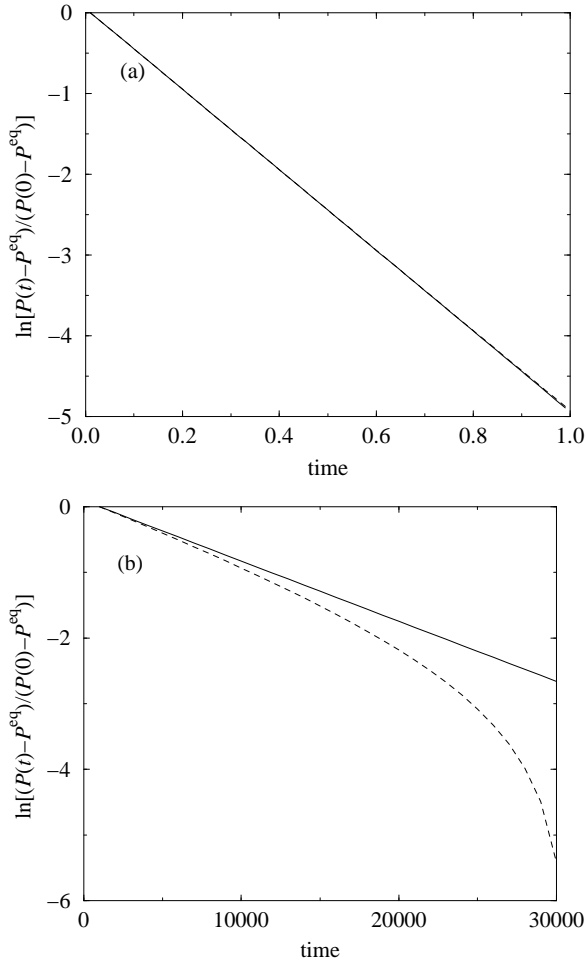


FIG. 9. Plots of Eq. (34) for LJ<sub>38</sub> in the microcanonical ensemble with the initial probability of the global minimum set to unity. Solid lines are Eq. (34) for the fcc funnel, and dashed lines are the equivalent for the icosahedral funnel. (a)  $E = -160 \epsilon$ , (b)  $E = -150 \epsilon$ . In (a) the lines coincide. The units of time are (a)  $10^{12} (m\sigma^2/\epsilon)^{1/2}$ , and (b)  $(m\sigma^2/\epsilon)^{1/2}$ .

To test the effect of having pruned the database, we lowered the threshold for removal of minima from an equilibrium probability of  $10^{-8}$  to  $10^{-12}$ , resulting in a larger remaining sample of 2289 minima. The net flow index picked out relaxation mode 17, whose eigenvalue was  $\lambda_{17} = -4.98 \times 10^{-12} (\epsilon/m\sigma^2)^{1/2}$ , i.e., the same as was obtained with the higher threshold. Replotting Fig.

9a also yielded the same result as before. We note that, even though this new sample is less than half the size of the full database, the lowest eigenvalues already clash with the precision of the “zero” eigenvalue. Hence, some pruning is essential for numerical tractability and desirable for computational speed, and it does not affect the result in this case.

At low energy, the interfunnel mode is easily identified. As the energy is raised and more processes become “unfrozen”, the distinction is somewhat less clear. Figure 9b shows Eq. (34) starting from the global minimum at  $E = -150 \epsilon$ . The database was pruned using an equilibrium probability threshold of  $10^{-8}$  and contained 3789 minima. Whilst the decay of  $P_{\text{fcc}}(t)$  obeys the linearized relationship, the evolution of  $P_{\text{icos}}(t)$  deviates from it increasingly as time progresses. This deviation is partly because minima outside the two funnels have non-negligible populations, so Eq. (32) does not hold, and also because  $P_{\text{icos}}(t)$  does not rise monotonically to its equilibrium value, but overshoots slightly and then decays. The net flow index picks out  $\lambda_{95} = -9.19 \times 10^{-5} (\epsilon/m\sigma^2)^{1/2}$  with  $f_{95}^{\text{fcc}} = 0.0859$  and  $f_{95}^{\text{icos}} = -0.0686$ . These values are considerably smaller than those obtained at  $E = -150 \epsilon$ . Although other modes may have a higher flow index for one funnel, the value for the other funnel is then either much smaller (indicating that the mode describes flow between one funnel and the non-funnel states), or of the same sign (indicating that flow is not *between* the funnels).

The slope of the solid line in Fig. 9b is  $-9.35 \times 10^{-5} (\epsilon/m\sigma^2)^{1/2}$ , which is not far from  $\lambda_{95}$ , but is actually closer to  $\lambda_{96} = -9.39 \times 10^{-5} (\epsilon/m\sigma^2)^{1/2}$ . However, mode 96 is only weakly interfunnel:  $f_{96}^{\text{fcc}} = 1.91 \times 10^{-4}$  and  $f_{96}^{\text{icos}} = -5.36 \times 10^{-4}$ . At relatively high energies, where minima outside the funnels come into play and the simplified scheme of Eq. (30) breaks down, the net flow index therefore still provides a convenient way of identifying the most important interfunnel relaxation mode and extracting the quantity  $(k_+ + k_-)$ . This method also has the advantage that it does not require evaluation of the master equation solution itself.

The equilibrium relationship Eq. (33) allows the separate rate constants  $k_+$  and  $k_-$  for interfunnel flow to be obtained from the eigenvalue. Table II shows  $k_+$  and  $k_-$  as a function of temperature in the canonical ensemble. At each temperature, the database was pruned using an equilibrium probability threshold of  $10^{-8}$ , and the table shows how many of the full sample of 6000 minima and 8633 transition states remained. At the lowest two temperatures, the pruning procedure removed all dead-end minima. The table also shows that the net flow indices for the interfunnel mode decrease in magnitude at the higher temperatures. This reduction is a result of the increasing involvement of higher-energy and non-funnel minima. Over the course of doubling the temperature,  $k_+$  changes by ten orders of magnitude. For argon parameters, the span of time scales is hundreds of nanoseconds to an hour.

TABLE II. Interfunnel rate constants for LJ<sub>38</sub> in the canonical ensemble.  $n'_{\min}$  and  $n'_{\text{ts}}$  are the numbers of minima and transition states remaining in the database after discarding minima with an equilibrium probability of less than  $10^{-8}$ .  $f^{\text{fcc}}$ ,  $f^{\text{icos}}$  and  $\lambda$  are the net flow indices and eigenvalue of the interfunnel mode.  $\lambda$ ,  $k_+$ , and  $k_-$  are tabulated in units of  $(\epsilon/m\sigma^2)^{1/2}$ .

$k_B T/\epsilon$	$n'_{\min}$	$n'_{\text{ts}}$	$\lambda$	$f^{\text{fcc}}$	$f^{\text{icos}}$	$k_+$	$k_-$
0.09	1770	4371	$-8.50 \times 10^{-15}$	0.282	-0.281	$7.36 \times 10^{-16}$	$7.77 \times 10^{-15}$
0.10	1770	4371	$-3.96 \times 10^{-13}$	0.399	-0.392	$7.48 \times 10^{-14}$	$3.22 \times 10^{-13}$
0.11	1783	4384	$-9.74 \times 10^{-12}$	0.471	-0.470	$3.22 \times 10^{-12}$	$6.52 \times 10^{-12}$
0.12	1809	4410	$-1.52 \times 10^{-10}$	0.500	-0.499	$7.39 \times 10^{-11}$	$7.80 \times 10^{-11}$
0.13	1851	4453	$-1.66 \times 10^{-9}$	0.483	-0.482	$1.06 \times 10^{-9}$	$5.97 \times 10^{-10}$
0.14	1978	4583	$-1.35 \times 10^{-8}$	0.438	-0.435	$1.00 \times 10^{-8}$	$3.53 \times 10^{-9}$
0.15	2264	4872	$-8.64 \times 10^{-8}$	0.381	-0.374	$7.09 \times 10^{-8}$	$1.54 \times 10^{-8}$
0.16	2620	5232	$-4.46 \times 10^{-7}$	0.320	-0.306	$3.92 \times 10^{-7}$	$5.36 \times 10^{-8}$
0.17	2985	5599	$-1.92 \times 10^{-6}$	0.259	-0.229	$1.77 \times 10^{-6}$	$1.52 \times 10^{-7}$
0.18	3363	5981	$-7.13 \times 10^{-6}$	0.202	-0.196	$6.77 \times 10^{-6}$	$3.57 \times 10^{-7}$

Figure 10 shows that, over the temperature range in Table II,  $k_+$  and  $k_-$  obey an Arrhenius temperature dependence law. Only very slight curvature is visible in the  $k_-$  results. Fitting to the form  $k = A \exp(-E_a/k_B T)$  gives the pre-exponential factors and activation energies for the forward and reverse processes:

$$\begin{aligned}
 k_+ : \text{fcc} \rightarrow \text{icos} & \quad A = 11.1 (\epsilon/m\sigma^2)^{1/2} & E_a = 4.12 \epsilon \\
 k_- : \text{icos} \rightarrow \text{fcc} & \quad A = 3.18 (\epsilon/m\sigma^2)^{1/2} & E_a = 3.19 \epsilon
 \end{aligned}$$

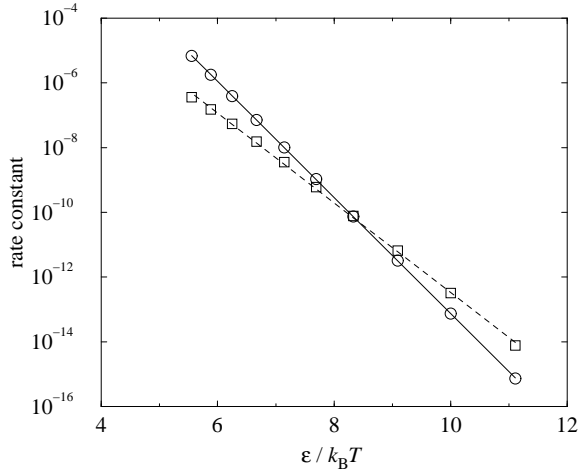


FIG. 10. Arrhenius plot of  $k_+$  (circles) and  $k_-$  (squares) for the interfunnel dynamics of LJ<sub>38</sub>. The lines are fits to the form  $k = A \exp(-E_a/k_B T)$ . The units of the rate constant are  $(\epsilon/m\sigma^2)^{1/2}$ .

Interestingly, the effective activation energy for  $\text{fcc} \rightarrow \text{icos}$  is close to the overall barrier on the lowest-energy path between the funnels, starting from the global minimum [5], which is  $4.22 \epsilon$ . This result suggests that the pathways passing over the highest-energy transition state on the lowest-energy pathway determine the interfunnel dynamics.  $E_a$  for  $\text{icos} \rightarrow \text{fcc}$ , however, is significantly lower than the overall potential barrier for the reverse

process, which is  $3.54 \epsilon$ , starting from the lowest-energy icosahedral minimum. The discrepancy can be attributed to the fact that more than one minimum in the icosahedral funnel is substantially occupied. Hence, the effective barrier from the icosahedral funnel should not be measured from the lowest-energy minimum in the icosahedral funnel, but with respect to a weighted average of the minimum energies,  $\sum_{i \in \text{icos}} P_i V_i$ . The slight curvature in the Arrhenius plot for  $k_-$  is a result of the temperature dependence of this average.

An alternative method for computing the rates for interfunnel conversion would be to calculate first the free energy barrier between the two funnels, and then the transmission coefficient for passage over this barrier [39]. The free energy barriers have been calculated for LJ<sub>38</sub> and were found to decrease as the temperature is increased towards that required for melting. Therefore, if this method is also to show an Arrhenius behaviour, the temperature dependence of the transmission coefficient must compensate that of the free energy barriers.

We have seen that the interfunnel rates drop dramatically as the temperature is lowered. At the same time, the increasing net flow indices show that the corresponding relaxation modes become more distinct from other processes. These features concur with Stillinger’s interpretation of  $\alpha$  processes in fragile liquids [28]. In this picture,  $\beta$  processes are faster and more localized in configuration space, whereas the  $\alpha$  processes, which become relatively slow at low temperatures, are thought to occur between “craters” (a similar concept to funnels) on the energy landscape. These differences give rise to a bifurcation of time scales, which is visible for LJ<sub>38</sub> in the eigenvalue spectra of Fig. 8. However,  $\alpha$  processes have been observed to have a non-Arrhenius temperature dependence, in contrast with the results of Fig. 10. The Arrhenius behaviour may be a genuine feature of the dynamics of the LJ<sub>38</sub> cluster, but could also be a limitation of the present approach. In particular, our incomplete database contains only a limited number of pathways between the two funnels, and competition be-



tween such paths would give rise to non-Arrhenius behaviour. We can study only a limited temperature range with our database, and the modelling of individual processes might not be sufficiently sophisticated. We note that Angelani et al. also observed unexpected Arrhenius behaviour in their master equation study of a fragile glass former [40,41].

### C. Equilibration

The progress of the probability vector towards equilibrium can be visualized using equilibration graphs [26,42–44]. Such a graph has a time axis, on which lines denote a group of states in local equilibrium with each other. Nodes join lines at the time that the corresponding groups first come into equilibrium, until there is just one group and the whole system has equilibrated. We define the time that minima  $i$  and  $j$  come into equilibrium as the smallest value of  $t$  after which

$$\frac{|P_i(t)P_j^{\text{eq}} - P_j(t)P_i^{\text{eq}}|}{\sqrt{P_i(t)P_j(t)P_i^{\text{eq}}P_j^{\text{eq}}}} \leq \xi \quad (36)$$

is always satisfied, and in the present work we set  $\xi = 0.01$ .

Figure 11 shows equilibration graphs for the six minima in each of the two funnels of LJ<sub>38</sub> that have the greatest equilibrium probability at  $E = -150\epsilon$ . They are numbered in order of increasing probability within each funnel. The initial vertical position of each minimum is taken as the integrated path length,  $S^{\text{gm}}$ , along the shortest path to the global minimum, making the two groups clearly distinguishable on this axis. Three microcanonical energies are plotted, spanning the range of applicability of our database. The sample was pruned using an equilibrium threshold of  $10^{-8}$  at each energy. The evolution of two initial probability vectors was considered: in the left-hand graphs, the initial probability of the global minimum is unity, and in the right-hand graphs the probability commences in the lowest-energy icosahedral minimum.

In each of the six graphs, the minima within a funnel come into equilibrium with each other before the separate funnels do so. This result explicitly demonstrates the longer time scale of the interfunnel dynamics. The order of equilibration within each funnel is the same at all three energies studied, irrespective of the funnel in which the probability is initiated. There is a small exception in graph (e), where minimum 6' in the icosahedral funnel equilibrates with 3' and 5' before it joins 1', 2' and 4'. Interestingly, the lowest-energy icosahedral minimum, 3', is one of the last minima to reach equilibrium within the

icosahedral funnel, presumably because of the high barriers surrounding it [5].

The equilibration of the fcc funnel is much more sensitive to the initial probability than that of the icosahedral funnel, in spite of the fact that the rate constants,  $k_+$  and  $k_-$ , are roughly equal at  $E = -160\epsilon$ . This difference in behaviour of the two funnels arises from the fact that the absolute probabilities of the minima in the fcc funnel, other than the global minimum itself, are several orders of magnitude smaller than those of the minima in the icosahedral funnel. Hence, small changes in probability due to transient flows easily disturb the equilibrium between minima in the fcc funnel, since distance from equilibrium is measured relative to the final probability by the left-hand side of inequality (36). When the cluster starts in the global minimum, the probability of the fcc minima decreases monotonically, and the minima within the funnel can equilibrate with each other rapidly. When the probability is initialized in the lowest-energy icosahedral minimum, however, the influx of probability to the fcc funnel must pass through the minima within the funnel on its way to the global minimum, and the transients must settle down almost completely before equilibrium is permanently established. This effect is reflected by the shift of the equilibration nodes of the fcc funnel to later times as one goes from the left-hand to right-hand side equilibration graphs in Fig. 11.

At sufficiently low energy, the global potential energy minimum must be the most populated state at equilibrium. However, we have seen that there is a kinetic bottleneck to entering its funnel. Hence, if the cluster is prepared in a liquid-like state, it is most likely to collapse into the icosahedral funnel, which is larger and structurally more similar to the liquid, even though it is not the equilibrium state. Over a sufficiently long time, the cluster must then convert to the global minimum. Our master equation model shows this behaviour clearly. Starting from a uniform distribution amongst the 25 highest-energy minima in the sample,  $P_{\text{fcc}}(t)$  and  $P_{\text{icos}}(t)$  were monitored as the system evolved towards equilibrium at the low energy of  $E = -160\epsilon$ . The results are shown in Fig. 12.

The initial states decay rapidly into other non-funnel states, and the two funnels experience a slow increase in population. Although some probability enters the fcc funnel, it reaches a plateau while the population of the icosahedral funnel continues to grow. This growth reaches a maximum before eventually decaying towards its equilibrium value, as the probability trickles into the global minimum. The icosahedral funnel acts as a kinetic trap, and only releases the cluster into the global minimum on a long time scale. We note that direct simulation of the trapping effect by standard MD would therefore be highly problematic.

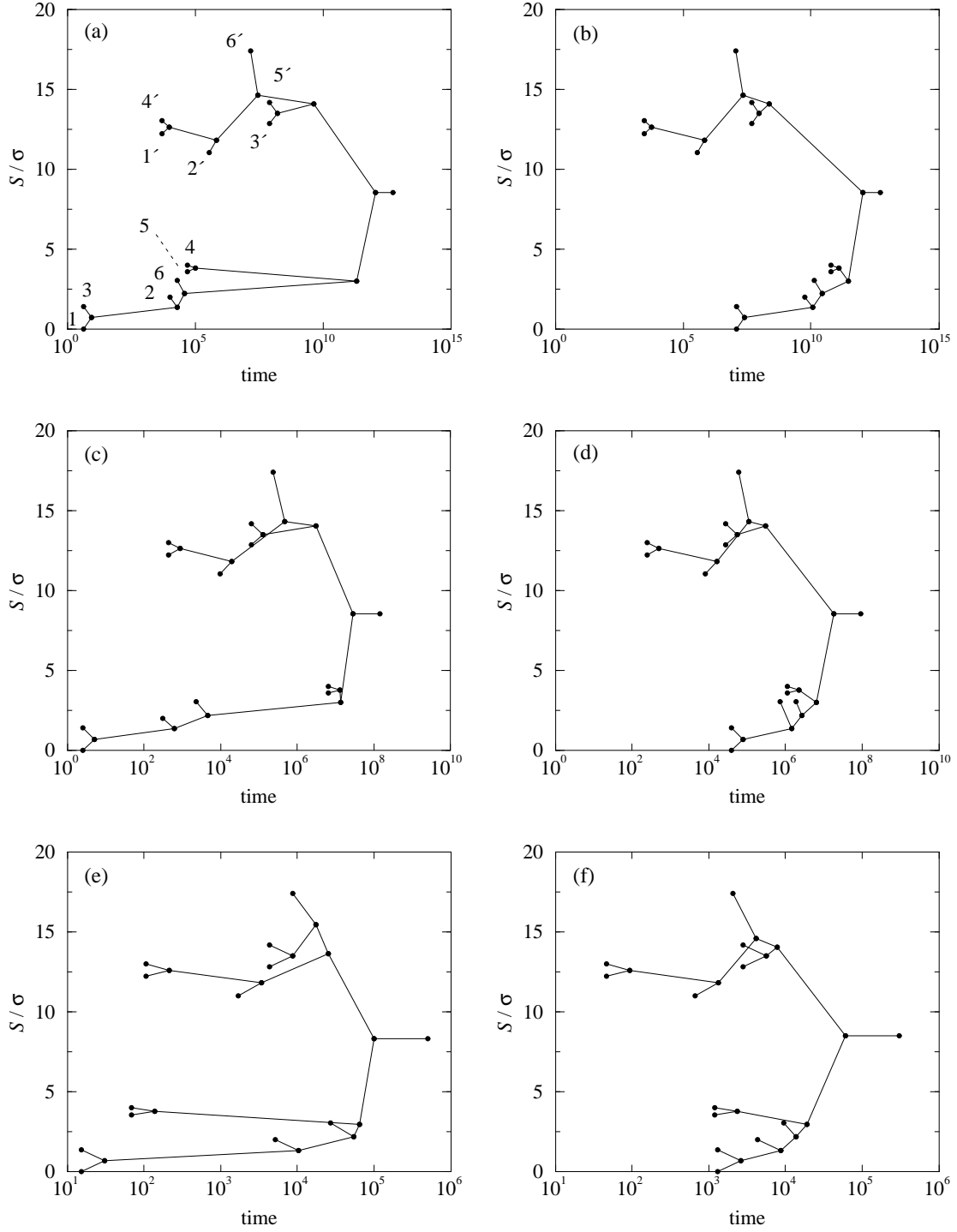


FIG. 11. Equilibration graphs for  $\text{LJ}_{38}$  in the microcanonical ensemble at three energies: (a) and (b)  $-160\epsilon$ , (c) and (d)  $-155\epsilon$ , (e) and (f)  $-150\epsilon$ . In each row, the left-hand graph is for the global minimum (labelled 1) having an initial probability of 1, and the right-hand graph is for the lowest-energy icosahedral minimum (labelled 3') having an initial probability of 1. Lines representing individual minima commence at a vertical position corresponding to the shortest integrated path length,  $S^{\text{gm}}$ , to the global minimum, and an arbitrary horizontal position. Nodes join lines when the corresponding states first come into equilibrium. In (a), unprimed numbers indicate minima in the fcc funnel, and primed numbers indicate minima in the icosahedral funnel. The time is in units of  $(m\sigma^2/\epsilon)^{1/2}$ .

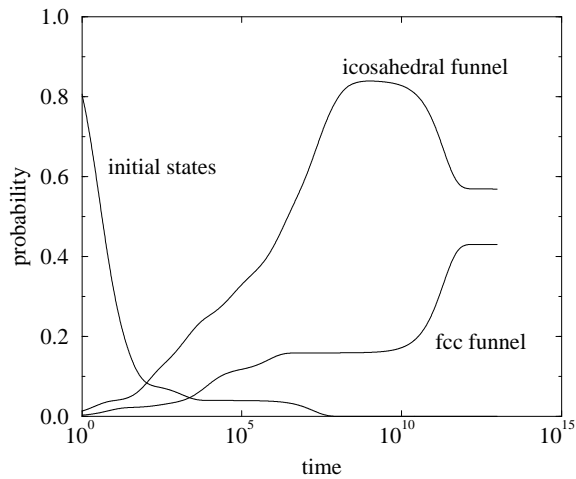


FIG. 12. Relaxation of LJ<sub>38</sub> from high-energy minima at a total energy of  $-160\epsilon$ , showing the fast and slow contributions to the final probability of the fcc funnel. The time is in units of  $(m\sigma^2/\epsilon)^{1/2}$ .

Although Fig. 12 unambiguously demonstrates the separate fast and slow contributions to the relaxation, the precise partitioning between the two funnels at the plateau stage can depend on the initial probability distribution. The distribution chosen here is rather artificial because our sample of minima does not extend into the liquid-like range. If we could release the system from a high-temperature liquid-like state, the fraction of probability flowing into the icosahedral funnel would probably be even larger because of the greater structural similarity of the liquid-like structures with the icosahedral rather than fcc minima. Although the fraction of fcc minima is already small in our database, it would be much smaller in a more comprehensive sample.

Two-stage dynamics have been observed experimentally in the folding of hen egg lysozyme, in which two routes to the native state have been postulated: one fast and direct, the other passing via partially folded conformations which act as kinetic traps and reorganize to the native state only slowly [45]. Conversely, the protein plasminogen activator inhibitor 1 rapidly folds to the active state, but converts to an inactive form on a much slower time scale [46], implying that the active state is not the global free energy minimum but is only metastable, like the icosahedral minima in LJ<sub>38</sub> at low energy. Similarly, human prion protein has two long-lived forms, whose relative stability can be adjusted by varying the pH. The time scale for conversion to the more stable form is of the order of days [47].

## V. SUMMARY

We have applied the master equation to the structural databases for M<sub>13</sub> and LJ<sub>38</sub> derived in previous work [4,36] to model relaxation processes in these atomic clusters. This approach can be applied to time scales far

longer than those accessible by direct simulation, and describes the behaviour of an equilibrating ensemble without the need to average over separate trajectories.

The harmonic approximation for the density of states of individual minima and transition states provides a simple but physically clear basis for calculating equilibrium properties and rate constants. Provided it is not applied at excessively high temperatures, it gives a qualitatively useful description of the thermodynamic and dynamic properties of the energy landscape.

As we predicted [4], relaxation to the global minimum is slower when the range of the potential is shorter. An optimal temperature for this relaxation is obtained by a compromise between the decreasing rates at low temperatures and the decreasing thermodynamic driving force at high temperatures. When the range of the potential is long, the cluster exhibits a wide temperature window over which relaxation is quite efficient. In contrast, when the range is short, small deviations from the optimal temperature hinder the rate appreciably.

Although the relaxation profiles of the total energy at fixed temperature do not appear to be well described by any of the commonly used empirical forms, the temperature dependence of the mean relaxation time followed an Arrhenius law for  $\rho = 14$  and a Vogel–Tammann–Fulcher law at  $\rho = 4$ . These results again reflect the greater uniformity of the short-range PES that was deduced in the landscape analysis.

Application of the analytic solution of the master equation to the low-energy database of LJ<sub>38</sub> required the removal of unimportant minima and transition states from the sample. “Dead-end” minima were removed if their equilibrium probability fell below a low threshold at the temperature of interest. The relaxation modes of the resulting database were analysed using a flow index to extract the rate of passage between the two funnels on the energy landscape at low temperatures. The equilibration patterns within and between the funnels clearly revealed the double-funnel structure. High-energy distributions relaxed preferentially into the secondary funnel of icosahedral minima rather than the close-packed funnel surrounding the global minimum. This behaviour stems from the greater structural similarity of the liquid to the icosahedral minima, which is reflected in the patterns of connectivity on the PES. Eventually, the cluster escaped from this kinetic trap into the global minimum, which is thermodynamically favoured at sufficiently low temperature.

## ACKNOWLEDGEMENTS

D.J.W. is grateful to the Royal Society and M.A.M. to the Engineering and Physical Sciences Research Council for financial support. J.P.K.D. is the Sir Alan Wilson Research Fellow at Emmanuel College, Cambridge.

- 
- [1] N. G. van Kampen, *Stochastic Processes in Physics and Chemistry* (North-Holland, Amsterdam, 1981).
- [2] F. H. Stillinger and T. A. Weber, Phys. Rev. A **25**, 978 (1982).
- [3] D. J. Wales, M. A. Miller, and T. R. Walsh, Nature **394**, 758 (1998).
- [4] M. A. Miller, J. P. K. Doye, and D. J. Wales, J. Chem. Phys. **110**, 328 (1999).
- [5] J. P. K. Doye, M. A. Miller, and D. J. Wales, (cond-mat/9903305).
- [6] M. A. Miller and D. J. Wales, (cond-mat/9904304).
- [7] R. E. Kunz, P. Blaudeck, K. H. Hoffmann, and R. S. Berry, J. Chem. Phys. **108**, 2576 (1998).
- [8] R. Czermanski and R. Elber, J. Chem. Phys. **92**, 5580 (1990).
- [9] W. H. Press, S. A. Teukolsky, W. T. Vetterling, and B. P. Flannery, *Numerical Recipes in FORTRAN*, 2 ed. (Cambridge University Press, Cambridge, 1992).
- [10] B. Vekhter and R. S. Berry, J. Chem. Phys. **106**, 6456 (1997).
- [11] M. A. Miller and D. J. Wales, J. Chem. Phys. **107**, 8568 (1997).
- [12] R. G. Gilbert and S. C. Smith, *Theory of Unimolecular and Recombination Reactions* (Blackwell, Oxford, 1990).
- [13] M. R. Hoare, Adv. Chem. Phys. **40**, 49 (1979).
- [14] G. Franke, E. R. Hilf, and P. Borrmann, J. Chem. Phys. **98**, 3496 (1993).
- [15] D. J. Wales, Mol. Phys. **78**, 151 (1993).
- [16] P. M. Morse, Phys. Rev. **34**, 57 (1929).
- [17] L. A. Girifalco and V. G. Weizer, Phys. Rev. **114**, 687 (1959).
- [18] L. A. Girifalco, J. Phys. Chem. **96**, 858 (1992).
- [19] D. J. Wales and J. Uppenbrink, Phys. Rev. B **50**, 342 (1994).
- [20] K. D. Ball and R. S. Berry, J. Chem. Phys. **109**, 8541 (1998).
- [21] K. D. Ball and R. S. Berry, J. Chem. Phys. **109**, 8557 (1998).
- [22] P. C. Haarhoff, Mol. Phys. **7**, 101 (1963).
- [23] J. P. K. Doye and D. J. Wales, J. Chem. Phys. **102**, 9659 (1995).
- [24] J. P. Rose and R. S. Berry, J. Chem. Phys. **98**, 3262 (1993).
- [25] N. D. Socci, J. N. Onuchic, and P. G. Wolynes, J. Chem. Phys. **104**, 5860 (1996).
- [26] J. P. K. Doye and D. J. Wales, J. Chem. Phys. **105**, 8428 (1996).
- [27] N. D. Socci and J. N. Onuchic, J. Chem. Phys. **101**, 1519 (1994).
- [28] F. H. Stillinger, Science **267**, 1935 (1995).
- [29] G. J. M. Koper and H. J. Hilhorst, Europhys. Lett. **3**, 1213 (1987).
- [30] R. G. Palmer, D. L. Stein, E. Abrahams, and P. W. Anderson, Phys. Rev. Lett. **53**, 958 (1984).
- [31] M. Skorobogatiy, H. Guo, and M. Zuckermann, J. Chem. Phys. **109**, 2528 (1998).
- [32] G. W. Scherer, J. Am. Ceram. Soc. **75**, 1060 (1992).
- [33] C. A. Angell, J. Non-cryst. Solids **131–133**, 13 (1991).
- [34] G. H. Golub and C. F. van Loan, *Matrix Computations*, 2nd ed. (John Hopkins University Press, Baltimore, 1989).
- [35] J. E. Jones and A. E. Ingham, Proc. R. Soc. A **107**, 636 (1925).
- [36] J. P. K. Doye, M. A. Miller, and D. J. Wales, J. Chem. Phys. **110**, 6896 (1999).
- [37] J. P. K. Doye, D. J. Wales, and M. A. Miller, J. Chem. Phys. **109**, 8143 (1998).
- [38] R. E. Kunz and R. S. Berry, J. Chem. Phys. **103**, 1904 (1995).
- [39] D. Chandler, *Introduction to Modern Statistical Mechanics* (Oxford University Press, Oxford, 1987).
- [40] L. Angelani, G. Parisi, G. Ruocco, and G. Vilianni, Phys. Rev. Lett. **81**, 4648 (1998).
- [41] L. Angelani, G. Parisi, G. Ruocco, and G. Vilianni, (cond-mat/9904125).
- [42] P. Sibani, J. C. Schön, P. Salamon, and J. Andersson, Europhys. Lett. **22**, 479 (1993).
- [43] J. C. Schön, Ber. Bunsenges. Phys. Chem. **100**, 1388 (1996).
- [44] J. C. Schön, H. Putz, and M. Jansen, J. Phys. Condensed Matter **8**, 143 (1996).
- [45] T. Kiefhaber, Proc. Natl. Acad. Sci. USA **92**, 9029 (1995).
- [46] D. Baker and D. A. Agard, Biochemistry **33**, 7505 (1994).
- [47] G. S. Jackson *et al.*, Science **283**, 1935 (1999).